JOURNAL OF GEOPHYSICAL RESEARCH: OCEANS, VOL. 118, 3202–3220, doi:10.1002/jgrc.20241, 2013

Predicting wave-induced ripple equilibrium geometry

Timothy Robert Nelson,[1] George Voulgaris,[2] and Peter Traykovski[3]

Received 8 March 2013; revised 9 May 2013; accepted 13 May 2013; published 28 June 2013.

[1] A comprehensive database of existing (since 1954) field and laboratory measurements of ripple geometry is compiled and combined with newly collected field data to examine the performance of ripple equilibrium predictors. Reanalysis of this enlarged ripple geometry data set reveals that ripples formed from monochromatic waves scale differently than ripples formed from random waves for many existing ripple predictors. Our analysis indicates that ripple wavelengths from the two data sets collapse into a single scaling when the semiorbital excursion and sediment grain diameter are used as normalizing factors. Ripple steepness remains relatively constant for both regular and irregular wave conditions, and it only slightly increases for shorter ripple wavelengths. These findings allowed for the development of a new equilibrium ripple predictor suitable for application in a wide range of wave and sediment conditions.

Citation: Nelson, T. R., G. Voulgaris, and P. Traykovski (2013), Predicting wave-induced ripple equilibrium geometry, *J. Geophys. Res. Oceans*, *118*, 3202–3220, doi:10.1002/jgrc.20241.

1. Introduction

[2] In the coastal ocean, ripples are formed by surface gravity waves traveling in water depths shallow enough for the oscillatory motion to be felt by the bed sediments. Once these oscillatory motions become large enough for the sediment grains to mobilize, the seabed begins to organize into a series of parallel ridges oriented perpendicular to the direction of wave propagation. These initial ripples have a small steepness (defined as the ratio of ripple height to wavelength) and are commonly known as rolling grain ripples [*Bagnold*, 1946]. Once the ripple steepness becomes greater than approximately 0.1, a vortex (eddy) forms on the lee side of the ripple that traps any sediment eroded from the ripple surface. Upon flow reversal, this sediment is ejected higher into the water column [*Bagnold*, 1946], contributing to increased sediment resuspension. In addition to their effect on resuspension, ripples play an important role in bottom friction as they affect turbulence levels and mean flow structure in the benthic boundary layer [e.g., *Grant and Madsen*, 1986] and also contribute to enhancing wave attenuation [e.g., *Ardhuin et al*., 2003]. More recently, *Madsen et al*. [2010] showed that wave-induced ripples could also alter the direction of the mean current close to the seabed, possibly having implications on the overall direction of sediment transport.

[3] Ripples can also act as a source (or sink) of seabed nutrients which are released to the overlying water column (or injected into the seabed) when they adjust their size and shape or are eroded during sheet flow conditions [e.g., *Precht and Huettel*, 2004]. Even under stable geometry, the pressure gradient forming between the high- (stoss) and low-pressure (lee) sides of the ripple can contribute to fluid permeating the ripple body, thereby flushing out nutrients or contaminants trapped in the space between the sedimentary particles that constitute the ripple [*Huettel et al*., 1998; *Rocha*, 2008]. Furthermore, the presence of ripples affects the use of acoustics in the marine environment as they facilitate the penetration of acoustic waves in the seabed [*Chotiros et al*., 2002; *Jackson et al*., 2002; *Thorsos and Richardson*, 2002], a condition that improves the detection of buried objects. On the other hand, they provide a backscattering surface that complicates seabed classification using acoustic backscattering techniques [e.g., *Voulgaris et al*., 1992; *Collins and Voulgaris*, 1993].

[4] Because of their importance, a number of studies have been carried out aiming at predicting the ripple dimensions for a given wave forcing. Earlier studies focused on identifying the geometric characteristics of ripples (wavelength and height) for a given wave orbital velocity, wave period, and sediment size [e.g., *Komar*, 1974; *Clifton*, 1976; *Nielsen*, 1981; *Grant and Madsen*, 1982 (GM); and references therein] and produced models that predict ripple wavelength and height assuming that a final form has been achieved (equilibrium ripple geometry). More recently, time-variable ripple prediction models [e.g., *Traykovski*, 2007 (Tr); *Soulsby et al*., 2012] have been developed that are able to

Additional supporting information may be found in the online version of this article.

[1]Department of Earth and Ocean Sciences, College of Arts and Sciences, University of South Carolina, Columbia, South Carolina, USA.
[2]Department of Earth and Ocean Sciences, Marine Science Program, College of Arts and Sciences, University of South Carolina, Columbia, South Carolina, USA.
[3]Applied Ocean Physics & Engineering Department, Woods Hole Oceanographic Institution, Woods Hole, Massachusetts, USA.

Corresponding author: T. R. Nelson, Department of Earth and Ocean Sciences, College of Arts and Sciences, University of South Carolina, Columbia, SC 29208, USA. (tnelson@geol.sc.edu)

2169-9275/13/10.1002/jgrc.20241

predict ripple dimensions at any time independently if the ripples are in equilibrium or not. These models, based on sediment transport principles, assume that when the seabed is not in equilibrium with the hydrodynamic forcing, the ripple reorganizes itself in order to achieve the equilibrium conditions. As the wave forcing changes in time so does the ultimate geometry the seabed tries to achieve (the equilibrium conditions) and prediction of this intermediate geometry is the goal of the time-dependent models which in turn depends on the definition of the equilibrium ripple predictor. To date, a large number of equilibrium models have been described in the literature. In Table 1 we present the references of 13 most commonly used spanning the years 1981–2009 as well as the type of data they used for deriving their corresponding model.

[5] The basis for many of the equilibrium ripple predictors is a set of dimensionless parameters based on the flow properties and sediment characteristics. This approach was first used by *Yalin and Russell* [1962] and further developed by others [*Carstens et al*., 1969; *Mogridge and Kamphuis*, 1972; *Dingler*, 1974; *Pedocchi and García*, 2009a (PG)]. The parameters commonly include wave bottom orbital velocity (u_b), wave period (T), median sediment grain diameter (D_{50}), sediment density (ρ_s), density of fluid (ρ_w), and gravity (g). This has led to the development of the following nondimensional parameters:

$$\left[T\nu/D_{50}^2,\ u_bD_{50}/\nu,\ \sqrt{(s-1)gD_{50}^3}/\nu,\ s-1,\ \phi\right] \qquad (1)$$

where $s=\rho_s/\rho_w$, ν is the kinematic viscosity of the fluid, and ϕ is the angle of repose which for sand is approximately equal to 32°. Various combinations of the above nondimensional numbers constitute the basis for many of the parameters commonly used in sediment dynamics such as the mobility number, the wave Reynolds number, the nondimensional sediment parameter, the wave period parameter, and the ratio of the wave orbital semiexcursion to the sediment grain size (A_b/D_{50}). A detailed description of the derivation of these parameters can be found in PG, while the corresponding equations are further described in section 2.

[6] The plethora of equilibrium ripple predictors, the different scaling used between them, and the lack of agreement among them emphasizes the point that the problem has not been resolved yet. The discrepancies could be attributed to differences in the data sets used in the development of these models, with some of them being obtained in the field and others in the laboratory; the quality of the data and the accuracy of the assumption that the data used represent real equilibrium conditions.

[7] Many of the early studies were primarily conducted in laboratory settings where the hydrodynamics can be easily controlled and ripples consistently observed [e.g., *Yalin and Russell*, 1962; *Kennedy and Falcon*, 1965; *Carstens et al*., 1969; *Lofquist*, 1978]. Later on, use of divers allowed for field observations under conditions conducive to the diver's safety and water visibility [e.g., *Inman*, 1957; *Miller and Komar*, 1980]. Subsequently, such observations were automated using underwater cameras which allowed for regular sampling intervals but were hindered by reduced visibility during energetic conditions [e.g., *Boyd et al*., 1988; *Powell et al*., 2000; *Xu*, 2005, and references therein]. During the past two decades, the use of a

Table 1. Equilibrium Ripple Predictors Examined in This Study

Model	Reference	Parameters	Data Type
NF	*Nielsen* [1981]	Mobility number	Field
NL	*Nielsen* [1981]	Mobility number Shields parameter	Lab
GM	*Grant and Madsen* [1982]	Shields parameter Dimensionless sediment parameter	Lab
Vr	*Van Rijn* [1993]	Mobility number	Field
MO	*Mogridge et al*. [1994]	Period parameter	Lab and field
WH	*Wiberg and Harris* [1994]	Orbital diameter Grain diameter	Lab and field
WM	*Wikramanayake and Madsen* [1994]	Mobility number Dimensionless sediment parameter	Field
SG	*Styles and Glenn* [2002]	Mobility number Dimensionless sediment parameter	Field
FF	*Faraci and Foti* [2002]	Wave Reynolds number Sediment Reynolds number Mobility number	Lab
GK	*Grasmeijer and Kleinhans* [2004]	Mobility number	Field
SW	*Soulsby and Whitehouse* [2005]	Orbital amplitude Grain diameter	Lab and field
Tr	*Traykovski* [2007]	Orbital diameter Settling velocity Radian wave frequency Orbital velocity	Field
PG	*Pedocchi and García* [2009a]	Dimensionless particle size Orbital velocity Settling velocity	Lab and field

stationary sector scanning sonar system has allowed for continuous sampling during long deployments regardless of water visibility [e.g., *Hay and Wilson*, 1994; *Traykovski et al*., 1999; *Voulgaris and Morin*, 2008; *Warner et al*., 2012] and wave activity levels. This proliferation of ripple measurements and the collection of additional data allow for testing the performance of existing models, their improvement, and possibly the development of a new model that better predicts wave-induced ripples in the marine environment.

[8] The objectives of this study are to (i) assemble all existing data (field and laboratory) of equilibrium ripples in a common database with commonly described hydrodynamic forcing; (ii) enrich this database with additional information that has become available; (iii) use this enriched database to evaluate already developed models; and (iv) if possible, present a new model that better fits all the data available to date. This is attempted by collecting existing data of ripple measurements from the published literature as well as including data from two new field experiments. All data assembled are presented in an electronic tabular form (see supporting information) for use by other investigators and enrichment over time as new data become available.

[9] The manuscript organization is so that section 2 presents a brief overview of the most widely used equilibrium ripple predictors. This is followed with a presentation of the ripple database and the source of the data (section 3). In section 4, an evaluation of the existing predictors against all the data assembled is carried out, while a discussion of their performance together with a new formulation is presented in section 5. Finally, in section 6 we present the conclusions of the study.

2. Existing Equilibrium Models

[10] In this section, we briefly present selective existing equilibrium models (see Table 1). The main criterion for their selection was their wide application in the literature and their diversity in terms of forcing parameters used. All of the models presented relate the ripple height and/or wavelength to hydrodynamic conditions usually normalized by parameters describing the sedimentary particles. At this junction it should be noted that different investigators have been defining the bottom orbital velocity parameter differently depending on the method they used to make their estimates (i.e., from direct velocity time series or wave height measurements) and the statistical representation adopted. For example, u_b in *Wikramanayake and Madsen* [1994] (WM) corresponds to standard deviation (σ) of oscillatory velocity, while in GM and *Styles and Glenn* [2002] (SG) the same parameter corresponds to amplitude of bottom orbital velocity which is defined as the $\sqrt{2}\sigma$. On the other hand, orbital velocities derived from significant wave height measurements correspond to 2σ [e.g., *Traykovski et al.*, 1999; *Wiberg and Sherwood*, 2008]. In order to avoid confusion, we have elected to define the parameters used through the adoption of appropriate subscripts that reveal the method of estimation as well as the relationship between different parameters (see Table 2).

[11] In the remainder of this section, the existing equilibrium models are described in subsections organized by the main parameter used in the model.

Table 2. Definitions and Subscripts Used for Wave Statistics

Subscript	Velocity[a]	Wave Height
rms	$u_{b,rms}=(\sigma_u{}^2+\sigma_v{}^2)^{1/2}$	$0.5H_{sig}$
eq(*br*)	$u_{b,eq}=[2(\sigma_u{}^2+\sigma_v{}^2)]^{1/2}$	$H_{rms}=H_{sig}/\sqrt{2}$
1/3	$u_{b,1/3}=2(\sigma_u{}^2+\sigma_v{}^2)^{1/2}$	H_{sig}
1/10	$u_{b,1/10}=1.27\times 2(\sigma_u{}^2+\sigma_v{}^2)^{1/2}$	$H_{1/10}=1.27H_{1/3}$

[a] $\sigma_u{}^2$ and $\sigma_v{}^2$ denote variance of wave-induced velocity.

2.1. Mobility Number

[12] One of the most common nondimensional parameters used to determine ripple geometry is the mobility number (ψ), which represents the ratio of mobilizing forces acting on the sediment to the stabilizing forces:

$$\psi = u_b^2/[(s-1)gD_{50}] \tag{2}$$

where s is the normalized sediment density, g is the acceleration due to gravity, and D_{50} is the median particle size.

[13] *Nielsen* [1981] proposed two sets of equations based on field/irregular and laboratory/regular wave conditions denoted as NF and NL, respectively. The equations developed for the regular monochromatic wave generated ripples were based on the studies of *Yalin and Russell* [1962], *Kennedy and Falcon* [1965], *Carstens et al*. [1969], *Mogridge and Kamphuis* [1972], *Dingler* [1974], *Nielsen* [1979], and used laboratory data from the Danish Hydraulic Institute. *Nielsen* [1981] found these ripples to be best described by the following equations:

$$\eta/A_{b,1/3} = 0.275 - 0.022\sqrt{\psi_{1/3}} \tag{3}$$

$$\lambda/A_{b,1/3} = 2.2 - 0.345\psi_{1/3}^{0.34} \tag{4}$$

where A_b is the wave orbital amplitude ($=2\pi u_b/T$) and T is the wave period.

[14] For field conditions, *Nielsen* [1981] used data collected from *Inman* [1957], *Dingler* [1974], and *Miller and Komar* [1980] to propose the following set of equations:

$$\eta/A_{b,1/3} = 21\psi_{1/3}^{-1.85}, \quad \psi_{1/3} > 10 \tag{5}$$

$$\lambda/A_{b,1/3} = \exp\left[\left(693 - 0.37\ln^8\psi_{1/3}\right)/\left(1000 + 0.75\ln^7\psi_{1/3}\right)\right] \tag{6}$$

[15] For $\psi_{1/3} < 10$, *Nielsen* [1981] recommends using the ripple height from equation (3). *Nielsen* [1981] also proposed a set of equations for ripple steepness based on the Shields parameter, which is further discussed in section 2.3.

[16] *Van Rijn* [1993] (Vr) also noted the potential scaling of ripple geometry with the mobility number. He used ripple dimensions measured under irregular waves from *Inman* [1957], *Dingler* [1974], *Ribberink and van Rijn* [1987], *Nieuwjaar and Van der Kaay* [1987], and *Van Rijn* [1987], and he suggested that equilibrium ripple geometry can be predicted by

$$\eta/A_{b,1/3} = \begin{cases} 0.22, & \psi_{1/3} \le 10 \\ 2.8 \times 10^{-13}\left(250 - \psi_{1/3}\right)^5, & 10 < \psi_{1/3} \le 250 \end{cases} \quad (7)$$

$$\eta/\lambda = \begin{cases} 0.18, & \psi_{1/3} \le 10 \\ 2.0 \times 10^{-7}\left(250 - \psi_{1/3}\right)^{2.5}, & 10 < \psi_{1/3} \le 250 \end{cases} \quad (8)$$

[17] *Grasmeijer and Kleinhans* [2004] (GK) analyzed the ripple measurements of *Inman* [1957], *Van Rijn et al*. [1993], *Van Rijn and Havinga* [1995], *Grasmeijer and van Rijn* [1999], and *Hanes et al*. [2001] as well as their own data collected off the coast of Egmond aan Zee, Netherlands, and to suggest that

$$\eta/A_{b,1/3} = \begin{cases} 0.275 - 0.022\psi_{1/3}^{0.5}, & \psi_{1/3} \le 10 \\ 2\psi_{1/3}^{-1}, & \psi_{1/3} > 10 \end{cases} \quad (9)$$

$$\eta/\lambda = \begin{cases} 0.14, & \psi_{1/3} \le 10 \\ -0.078 + 0.355\psi_{1/3}^{-0.221}, & \psi_{1/3} > 10 \end{cases} \quad (10)$$

[18] One commonality between the latter two models (i.e., Vr and GK) is that wave steepness is assumed to be constant (0.14 and 0.18 for the GK and Vr models, respectively) for low energy flows, while it decreases under more energetic wave activity.

2.2. Mobility Number and Dimensionless Sediment Parameter

[19] Another nondimensional parameter used to determine ripple geometry is the ratio of the mobility number (ψ) and the dimensionless sediment parameter (S_*) with the latter being defined as

$$S_* = \sqrt{(s-1)gD_{50}^3}/4\nu \quad (11)$$

[20] This parameter was first proposed by WM and later adopted by SG. In addition to taking into account the sediment properties and orbital wave forcing, this parameter also accounts for water viscosity (ν) and therefore requires knowledge of the water temperature, salinity, and pressure (i.e., water depth).

[21] WM utilized the data from the field measurements of *Inman* [1957], *Miller and Komar* [1980], and *Nielsen* [1984] and suggested the following equations to predict ripple height and wavelength:

$$\eta/A_{b,rms} = \begin{cases} 0.27(\psi_{rms}/S_*)^{-1/2}, & \psi_{rms}/S_* \le 3 \\ 0.52(\psi_{rms}/S_*)^{-1.1}, & \psi_{rms}/S_* > 3 \end{cases} \quad (12)$$

and

$$\lambda/A_{b,rms} = \begin{cases} 1.70(\psi_{rms}/S_*)^{-1/2}, & \psi_{rms}/S_* \le 3 \\ 2.10(\psi_{rms}/S_*)^{-0.7}, & \psi_{rms}/S_* > 3 \end{cases} \quad (13)$$

[22] Equations (12) and (13) were later revised by SG who incorporated additional field data from *Wiberg and Harris* [1994] (WH) and *Traykovski et al*. [1999] to derive an improved fit between data and model so that

$$\eta/A_{b,eq} = \begin{cases} 0.30\left(\psi_{eq}/S_*\right)^{-0.38}, & \psi_{eq}/S_* \le 2 \\ 0.48\left(\psi_{eq}/S_*\right)^{-1.1}, & \psi_{eq}/S_* > 2 \end{cases} \quad (14)$$

$$\lambda/A_{b,eq} = \begin{cases} 1.95\left(\psi_{eq}/S_*\right)^{-0.30}, & \psi_{eq}/S_* \le 2 \\ 2.80\left(\psi_{eq}/S_*\right)^{-0.82}, & \psi_{eq}/S_* > 2 \end{cases} \quad (15)$$

where ψ_{eq} is the mobility number attained from calculating u_b using the root-mean-square (*rms*) wave height (or $\sqrt{2}$ times the variance of flow velocity). At this juncture, it should be noted that equations (14) and (15) vary slightly from those in the original manuscript of SG due to a typographical error in the original manuscript (Styles, personal communication).

2.3. Shields Parameter Based Equilibrium Models

[23] While *Nielsen* [1981] found that ripple wavelength and height were best described by the mobility number, he proposed a separate equation for steepness, which is based on the wave *Shields* [1936] parameter (θ). For regular laboratory waves, *Nielsen* [1981] suggested

$$\eta/\lambda = 0.182 - 0.24\theta_{1/3}^{1.5} \quad (16)$$

while for irregular field waves, he proposed

$$\eta/\lambda = 0.342 - 0.34\sqrt[4]{\theta_{1/3}} \quad (17)$$

where θ is defined as

$$\theta = 0.5 f_w u_b^2/[(s-1)gD_{50}] \quad (18)$$

with the wave friction coefficient (f_w) defined as [*Jonsson*, 1966]

$$f_w = \begin{cases} \exp\left[5.213 \cdot (2.5D_{50}/A_b)^{0.194} - 5.977\right], & A_b/(2.5D_{50}) > 1.57 \\ 0.3, & A_b/(2.5D_{50}) \le 1.57 \end{cases} \quad (19)$$

[24] GM utilized data from *Carstens et al*. [1969] and found a relationship between the Shields parameter and ripple dimensions that defines increasing ripple wavelengths with increasing Shields parameter value up to $1.8S_*^2$ and decreasing wavelengths thereafter. This led to a new set of equations for the prediction of equilibrium ripples:

$$\eta/A_{b,eq} = \begin{cases} 0.22\left(\theta_{eq}/\theta_{cr}\right)^{-0.16}, & \theta_{eq}/\theta_{cr} \le 1.8S_*^2 \\ 0.48S_*^{0.6}\left(\theta_{eq}/\theta_{cr}\right)^{-1.5}, & \theta_{eq}/\theta_{cr} > 1.8S_*^2 \end{cases} \quad (20)$$

$$\eta/\lambda = \begin{cases} 0.16\left(\theta_{eq}/\theta_{cr}\right)^{-0.04}, & \theta_{eq}/\theta_{cr} \le 1.8S_*^2 \\ 0.28S_*^{0.6}\left(\theta_{eq}/\theta_{cr}\right)^{-1.0}, & \theta_{eq}/\theta_{cr} > 1.8S_*^2 \end{cases} \quad (21)$$

where θ_{cr} is the critical Shields parameter for sediment mobility.

2.4. Period Parameter

[25] *Mogridge et al*. [1994] (MO) used the data of *Bagnold* [1946], *Inman* [1957], *Yalin and Russell* [1962],

Kennedy and Falcon [1965], *Horikawa and Watanabe* [1967], *Carstens et al*. [1969], *Mogridge* [1972], *Dingler* [1974], *Miller and Komar* [1980], and *Willis et al*. [1993] to develop a set of equations that provide an upper limit on the ripple dimensions rather than an actual prediction. These upper limits were related to a newly defined parameter χ as follows:

$$\eta/D_{50} = 10^{8.542-10.822\chi^{0.03967}} \tag{22}$$

$$\lambda/D_{50} = \begin{cases} 1394, & \chi < 1.5\times10^{-7} \\ 10^{13.373-13.772\chi^{0.02054}}, & \chi \geq 1.5\times10^{-7} \end{cases} \tag{23}$$

where χ relates the sediment size to wave period as follows:

$$\chi = \rho_w D_{50}/\left(\rho_s g T^2\right) \tag{24}$$

[26] While *Nielsen* [1981] argued that this parameter does not have any physical meaning, MO suggested that the wave period directly reflects velocities, accelerations, and forces of the oscillatory motion. MO found η/D_{50} to be accurately described by a single equation; however, the ripple wavelength diverges at χ values smaller than 1.5×10^{-5}. They found that field data best conforms to a constant λ/D_{50} value of 1394.

2.5. Orbital Excursion and Grain Size

[27] Another parameter widely used to predict ripple dimensions is the wave orbital excursion (d_o=$2A_b$) normalized by the sediment grain diameter (d_o/D_{50}). *Clifton* [1976] and *Clifton and Dingler* [1984] first observed a dependence of ripple characteristics to different parameters depending on the value of the ratio of wave orbital excursion to grain size (d_o/D_{50}). For smaller values of d_o/D_{50}, these orbital ripples have a wavelength that scales with the wave orbital diameter.

[28] WH proposed a set of equations based on orbital-suborbital-anorbital classification scheme using laboratory and field data from *Inman* [1957], *Kennedy and Falcon* [1965], *Carstens et al*. [1969], *Mogridge and Kamphuis* [1972], and *Dingler* [1974]. The original WH model requires an iterative approach, but *Malarkey and Davies* [2003] presented a modification that simplifies the estimation of ripple characteristics:

$$d_{o,1/3}/\eta = \exp\left[C_1 - \sqrt{C_2 - C_3\,\ln\left(d_{o,1/3}/\lambda\right)}\right] \tag{25}$$

$$\lambda = \begin{cases} 0.62d_{o,1/3}, & d_{o,1/3}/\eta_{ano} < 20 \\ 535D_{50}\exp\left[-\ln\left(\dfrac{0.62d_{o,1/3}}{535D_{50}}\right)\dfrac{\ln\left(0.01d_{1/3}\right)}{\ln(5)}\right], & 20 \leq d_{o,1/3}/\eta_{ano} \leq 100 \\ 535D_{50}, & d_{o,1/3}/\eta_{ano} < 100 \end{cases} \tag{26}$$

where $d_{o,1/3}/\eta_{ano}$ is calculated using equation (25) with $\lambda = \lambda_{ano} = 535D_{50}$, C_1=7.59, C_2=33.60, C_3=10.53, $d_{o,1/3}$ is the significant wave orbital diameter, ($_{ano}$) indicates the anorbital ripple geometry, and the equilibrium η is found using λ in equation (25).

[29] *Soulsby and Whitehouse* [2005] (SW) used data from an extensive database of published ripple dimensions, including the ones mentioned earlier, to suggest that scaling of ripple geometry characteristics with the ratio of wave orbital semiexcursion of the highest 1/10 velocities ($A_{b,1/10} = 1.27A_{b,1/3}$) to the median particle diameter (D_{50}) provides the least scatter suggesting

$$\lambda/A_{b,1/10} = \left(1 + 1.8710^{-3}A_{b,1/10}/D_{50}\left\{1 - \exp\left[-\left(2\times10^{-4}A_{b,1/10}/D_{50}\right)^{1.5}\right]\right\}\right)^{-1} \tag{27}$$

$$\eta/\lambda = 0.15\left\{1 - \exp\left[-\left(5000D_{50}/A_{b,1/10}\right)^{3.5}\right]\right\} \tag{28}$$

2.6. Orbital Excursion (d_o) and w_s/ω

[30] Similar to the predictors described earlier, Tr also noted that ripples do tend to scale with orbital diameter. However, his predictor assumes that the cutoff for orbital ripples (i.e., where ripples scale with the orbital diameter) occurs at a value of $u_{b,1/3}/w_s \leq 4.2$. Above this value, the ripples scale as a function of sediment settling velocity (w_s) and wave radian frequency (ω=$2\pi/T$). Tr found strong agreement between ripples observed off the coast of Martha's Vineyard [*Traykovski et al*., 1999; Tr], using the following set of equations:

$$\lambda = \begin{cases} 0.75d_{o,1/3}, & u_{b,1/3}/w_s \leq 4.2 \\ 6.3w_s/\omega, & u_{b,1/3}/w_s > 4.2 \end{cases} \tag{29}$$

where w_s is the particle settling velocity calculated from *Gibbs et al*. [1971]. Assuming a constant value for ripple steepness of $\eta/\lambda = 0.16$, the ripple equilibrium height is obtained as

$$\eta = \begin{cases} 0.12d_{o,1/3}, & u_{b,1/3}/w_s \leq 4.2 \\ 1.008w_s/\omega, & u_{b,1/3}/w_s > 4.2 \end{cases} \tag{30}$$

[31] It is worth noting that according to equations (29) and (30), for $u_{b,1/3}/w_s > 4.2$, ripple geometry depends solely on wave period and sediment settling velocity. This follows the observations of MO and might explain some of the scatter and different trends observed in their predictor.

2.7. Reynolds Numbers

[32] *Faraci and Foti* [2002] (FF) derived a relationship based on the wave (Re_w) and sediment (Re_d) Reynolds numbers, respectively, defined as

$$Re_w = u_{b,1/3}A_{b,1/3}/\nu \tag{31}$$

$$Re_d = u_{b,1/3}D_{50}/\nu \tag{32}$$

[33] Using ripple geometry data from wave tank experiments with both monochromatic and irregular waves, they developed the following expressions for ripple wavelength and height:

$$\lambda/A_{b,1/3} = 12.0613 Re_d Re_w^{-0.68} \tag{33}$$

$$\eta/A_{b,1/3} = \left(1 - 0.022\psi_{1/3}^{1/2}/0.275\right)\exp\left[-\left(0.0076 Re_w^{0.5} + 0.1681\right)\right] \tag{34}$$

[34] Although they found the measured ripple steepness to agree with *Nielsen* [1979], they also noticed that the average steepness was 0.18, which corresponds to fully developed vortex ripples. They suggested that ripple steepness must depend on the angle of repose (ϕ) and recommended, as in *Nielsen* [1979, 1981], that

$$\eta/\lambda = 0.32\ \tan\phi \tag{35}$$

which leads to $\eta/\lambda = 0.185$ if we assume an angle of repose of 30°.

2.8. Orbital Velocity/Settling Velocity

[35] PG used published ripple dimension data as well as data from a wave tunnel experiment [*Pedocchi and García*, 2009b] to suggest that ripple dimensions should be related to the ratio of $u_{b,1/3}/w_s$ for three different grain size regimes based on the particle Reynolds number (Re_p). The latter relates to the dimensionless particle size parameter (S_*) as follows:

$$Re_p = \sqrt{(s-1)gD_{50}^3}/\nu = 4S_* \tag{36}$$

[36] Their study led to the following sets of equations:

$$\lambda/D_{50} = \begin{cases} 0.65\left[\left(0.050 u_{b,1/3}/w_s\right)^2 + 1\right]^{-1}, & Re_p \geq 13 \\ 0.65\left[\left(0.040 u_{b,1/3}/w_s\right)^2 + 1\right]^{-1}, & 9 \leq Re_p < 13 \\ 0.65\left[\left(0.054 u_{b,1/3}/w_s\right)^3 + 1\right]^{-1}, & Re_p < 9 \end{cases} \tag{37}$$

$$\eta/D_{50} = \begin{cases} 0.1\left[\left(0.055 u_{b,1/3}/w_s\right)^3 + 1\right]^{-1}, & Re_p \geq 13 \\ 0.1\left[\left(0.055 u_{b,1/3}/w_s\right)^4 + 1\right]^{-1}, & 9 \leq Re_p < 13 \\ 0.1\left[\left(0.055 u_{b,1/3}/w_s\right)^5 + 1\right]^{-1}, & Re_p < 9 \end{cases} \tag{38}$$

where w_s is the particle settling velocity calculated using the method of *Dietrich* [1982]. These equations are divided into three grain size regions with $Re_p = 13$ corresponding to 220 μm and $Re_p = 9$ corresponding to 177 μm at 20°C.

3. Data Availability

3.1. Existing Data Sources

[37] Numerous experiments on oscillatory flow ripples have been carried out over the years resulting in a large number of ripple wavelength and height data for a variety of wave conditions and sediment sizes. Various subsets of these data were used in the development of the equilibrium prediction models described in section 2. As part of this study, all data available (see Table 3) are compiled into a single database to be used for the production of a more comprehensive formulation for ripple equilibrium dimensions that is not experiment or site specific. The ripple geometry data found in the literature include descriptions of hydrodynamic forcing, sediment type, and ripple dimensions; however, not all sources provide the same parameters, and for this reason, all hydrodynamic data have been converted to commonly defined parameters: significant orbital velocity ($u_{b,1/3}$), wave period (T), median grain diameter (D_{50}), water temperature ($Temp$), water density (ρ_w), sediment density (ρ_s), water depth (h), salinity (S), ripple wavelength (λ), and ripple height (η). For the experiments where wave forcing was listed as wave height alone, the significant (1/3) bottom orbital velocity was calculated using linear wave theory:

$$u_{b,1/3} = H_{1/3}\omega[2\sinh(kh)] \tag{39}$$

where ω is the wave radial frequency, $H_{1/3}$ is the significant wave height, k is the wave number, and h is the local water depth.

[38] Another parameter, which is often omitted but required by several of the predictors presented in section 2, is the water viscosity (ν). When water temperature, salinity, and water depth data are provided, the viscosity is calculated from these values, otherwise a water temperature of 20°C and a salinity of 0 are assumed for laboratory experiments. For field experiments, temperature and salinity information obtained at a nearby buoy from the national data buoy center (http://www.ndbc.noaa.gov/) is used. When no historical data exist, an average (climatological) value of water temperature for the specified month(s) of the experiment is taken and if no salinity is recorded, a value of 35 psu is assumed.

3.2. New Data Sources

[39] In addition to the existing data described earlier, new data sets from two experimental sites, representing different wave environments and sediment characteristics, are also included in this database and subsequent analysis. Both sites are located in the South Atlantic Bight offshore South Carolina and Georgia (USA), respectively. The first field data set is from the shelf on the northern part of South Carolina (USA) off Long Bay (33°43.35′N, 78°46.75′W; Figure 1). These data were collected as part of the U.S. Geological Survey's South Carolina Coastal Erosion Study, which took place from October 2003 to April 2004 [*Sullivan et al.*, 2006; *Schwab et al.*, 2009; *Warner et al.*, 2012]. The seabed sediment at this site consists of fine to medium quartz sand with a median grain diameter (D_{50}) of 177 μm. Data from the period 30 January to 15 March 2004 are used in this study as this provides the most complete record of hydrodynamic and bed form wavelength data. The second data set is from the continental shelf off the coast of Georgia (USA; 31°22.343′N, 80°34.073′W; Figure 2). The seabed at this site consists of medium to coarse sand with a mean diameter of 388 μm. Two periods of simultaneous hydrodynamic and bed form imagery data collection are used, corresponding to 16 September to 7 October 2007 and 13 December 2007 to 15 February 2008. These periods include several sediment mobilization events where bed forms change dimension and orientation (Figure 2). The

Table 3. Data Sources Used in This Study Also Included in the Database[a]

Source	Setup	Wave Condition[b]	$s = \rho_s/\rho_w$	T (s)	$u_{b,1/3}$ (cm/s)	Depth (m)	λ (cm)	η (cm)
Inman [1957]	Field	IRG	2.65	0.5–16	10–310	0.03–33.5	4.3–125	0.5–22.9
Yalin and Russell [1962]	Flume	REG	1.48, 1.19, 2.7	1–4.3	9.5–50.5	0.7	2–15.2	N/A
Kennedy and Flacon [1965]	Flume	REG	1.03, 1.35, 2.67	1.1–7.3	0.6–42.1	0.4–5.8	1.7–8.6	0.1–1.7
Carstens et al. [1969]	Tunnel	REG	2.47–2.65	3.3–3.8	12.9–79.6	0.3	8.8–46.3	0.5–6.9
Mogridge and Kamphuis [1972]	Tunnel	REG	2.65	1–14.1	1.4–68.5	1.2	3–101.7	0.4–18.4
	Flume							
Dingler [1974]	Field	IRG	2.65	6.9–13.9	19.8–127.3	0.5–8	7.2–79	0.1–13.5
	Tunnel	REG	2.65	1.7–5	14–68	1.2, 1.7	6.9–39	0.8–6.3
Lofquist [1978]	Tunnel	REG	2.65	1.6–16	17.7–77.1	0.3	3.8–72.5	1.6–15.5
Nielsen [1979]	Flume	REG	2.65	1, 1.3, 1.7, 3	6.3–51.3	0.4	2.5–46	0.4–2.7
Miller and Komar [1980]	Field	IRG	2.65	6–18.2	4–158.5	3.1–32.9	7.6–27.1	N/A
Bosman [1981]	Tunnel	REG	2.65	0.5–20	13–78	0.4	1.7–30	0.4–4.5
Du Toit and Van Rijn [1981]	Flume	REG	2.65	3.2–5.8	8.8–27.7	0.48	6.5–25.3	1–4.4
Hayakawa et al. [1983]	Tunnel	REG	2.65	4, 5, 6	31.5–54.7	N/A	25.7–34.1	2.7–3.8
Nielsen [1984]	Field	IRG	2.65	5.3–14.4	39.1–113.6	0.8–1.8	5–150	0.5–20
Steetzel [1984]	Tunnel	REG	2.65	3–7	20–50	N/A	13–31.5	2–4.5
		IRG						
Sakakiyama et al. [1986]	Flume	REG	2.65	3–12	17–197	N/A	14.3–148	1.9–11.7
Nieuwjaar and Van der Kaay [1987]	Tunnel	IRG	2.65	2.4, 2.5	21.2–47.6	N/A	8.5–9.3	1.1–1.8
Ribberink and Van Rijn [1987]	Tunnel	IRG	2.65	2–5	38.5–71.3	N/A	8–13.5	1–1.8
Boyd et al. [1988]	Field	IRG	2.65	3.1–11.4	6.4–121.6	9.6–12.5	7–24	N/A
Van Rijn [1987]	Tunnel	IRG	2.65	4.6–6.3	62.2–178.2	N/A	20	0.1–2
Southard et al. [1990]	Duct	REG	2.65	3.1–19.3	10–100	0.2	12–196	2.1–23.9
Van Rijn [1993]	Flume	IRG	2.65	2.2–2.7	13.7–36.1	0.5	6–20	0.6–2.9
Ribberink and Al-Salem [1994]	Tunnel	REG	2.65	2–12	20–150	0.8	8.4–270	0.3–35
Van Rijn and Havinga [1995]	Basin	REG	2.65	2.1–2.3	14.4–29.9	0.4	5.9–11.1	0.6–1.4
		IRG						
Li and Amos [1998]	Field	IRG	2.65	8–12.8	1.9–28.8	38.7–40	7.7–15.4	0.8–2.2
Grasmeijer and van Rijn [1999]	Flume	IRG	2.65	2.3	27–52.1	0.3–0.6	3.8–8.3	0.5–1.3
Hume et al. [1999]	Field	IRG	2.65	11	20–75	25	40–90	3–13
Traykovski et al. [1999]	Field	IRG	2.65	5.1–14.3	4.6–49.2	11.8–13.7	36.7–107	N/A
Doucette [2000]	Field	IRG	2.65	4.7–12.2	17–102.8	0.3–1.7	5–70	0.5–11
Khelifa and Ouellet [2000]	Basin	REG	2.65	0.9–1.4	8.2–25.5	0.3	2.8–12.1	0.4–1.7
Williams et al. [2000]	Flume	REG	2.65	3.5–5	19–69	6.5	8–35	1.5–6
Faraci and Foti [2001]	Flume	REG	1.2,	1.3–4.2	5.4–86	0.2, 0.3	3.7–12	0.4–2.1
		IRG	2.65					
Hanes et al. [2001]	Field	IRG	2.65	7.1–19.7	9.2–271.8	1.6–6.8	6–270	0.4–9.9
O'Donoghue and Clubb [2001]	Tunnel	REG	2.65	2–15	18–106	0.6	6–121	0.9–19.4
		IRG						
Ardhuin et al. [2002]	Field	IRG	2.65	11.4–13.8	37–67	19.7–27.6	77–137	N/A
Doucette [2002]	Field	IRG	2.65	2.2–12.2	15.6–59.1	0.2–1.1	8–91	2–14
Faraci and Foti [2002]	Flume	REG	2.65	1.3–4.2	12.7–35	0.3	4.4–10.7	0.7–2.1
		IRG						
Sleath and Wallbridge [2002]	Tunnel	REG	2.65	2.8–6.8	8–164	0.3	10–50	1.7–9
Thorne et al. [2002]	Flume	IRG	2.65	4–6	25.7–65.8	4.5	26.2–51.3	4–6.5
Grasmeijer and Kleinhans [2004]	Field	IRG	2.65	4–10.5	23–98.5	2	19–200	0.7–10
Williams et al. [2004]	Flume	IRG	2.65	4–6	13.1–102.6	4, 4.5	20–104	1–7
Dumas et al. [2005]	Tunnel	REG	2.65	7.9–11	20.1–165.3	0.7	6.5–723.8	0.4–53.2
Smith and Sleath [2005]	Tray	REG	2.65	0.9–3.8	15.6–49	0.4	3.5–30.7	0.3–4.1
Xu [2005]	Field	IRG	2.65	8.8–18.3	15.6–43.8	15	4.6–7.5	N/A
Brown [2006]	Flume	REG	2.65	4, 6, 8	26.5–66.8	4.6	5.5–23	0.2–2.3
		IRG						
Doucette and O'Donoghue [2006]	Tunnel	REG	2.65	2–12.5	29.8–146.6	0.5	8.7–82.3	1.3–12.8
		IRG						
O'Donoghue et al. [2006]	Tunnel	REG	2.65	3.1–12.5	27–88	0.5, 0.8	11.4–110.7	1.5–13.9
		IRG						
Traykovski [2007]								
Martha's Vineyard Coastal Observatory 2002	Field	IRG	2.65	1–12.9	5.5–133.1	12–13.9	10–127	N/A
Martha's Vineyard Coastal Observatory 2005	Field	IRG	2.65	6.2–11.6	12–80.9	12.3–13.7	39.4–127.8	2.9–16.6
Pedocchi and García [2009b]	Tunnel	REG	2.65	2–25	20–100	0.6	5–180	0.6–19
Nelson and Voulgaris[c]								
Long Bay, SC	Field	IRG	2.65	4.8–12.7	6.6–43.9	8.2–10.6	7–22.4	N/A
Georgia Shelf	Field	IRG	2.65	6.5–12.3	3.1–45.6	26.1–29	9.5–75.8	N/A

[a]See supporting information.
[b]REG (IRG) denote regular (irregular) wave conditions.
[c]Nelson and Voulgaris (submitted manuscript, 2013).

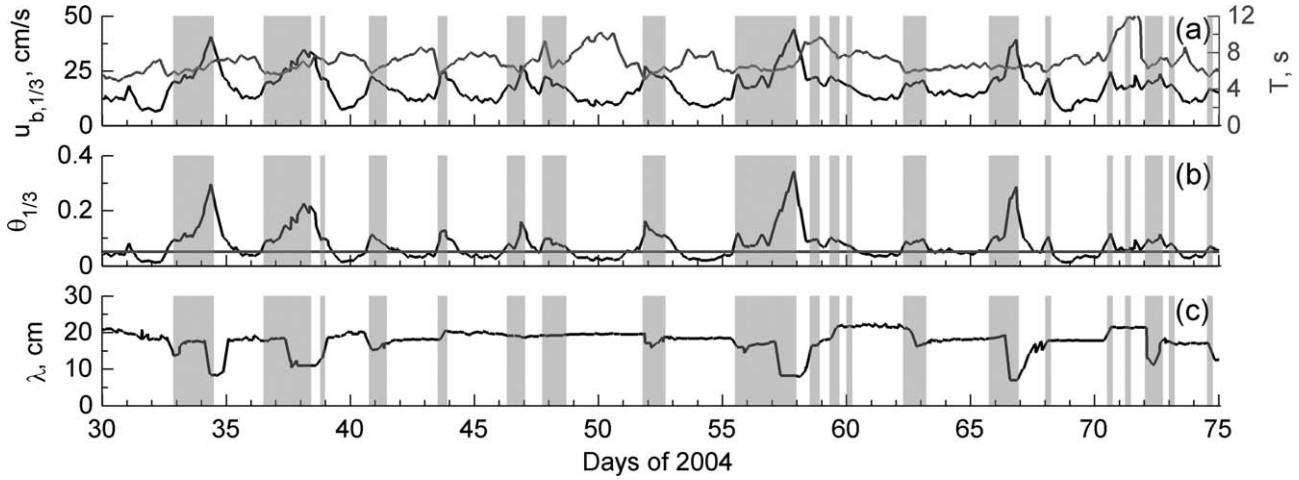

Figure 1. Time series of data collected in Long Bay, South Carolina (USA) during 2004: (a) significant wave orbital velocity (black) and wave period (gray); (b) wave Shields parameter (black) and critical Shields parameter (gray); and (c) measured ripple wavelength. The shaded areas indicate periods when $0 < d\theta/dt < 0.1\theta_{1/3}(t)/T_k(t)$ and $\theta_{1/3} > 1.5\theta_{cr}$ (see text).

detailed description of the experimental setup, hydrodynamic conditions, ripple evolution description, as well as the methodologies used is presented in detail by T. R. Nelson and G. Voulgaris [Temporal and spatial evolution of wave-induced ripple geometry: Regular versus irregular ripples, submitted to *Journal of Geophysical Research*, 2013] and by *Voulgaris and Morin* [2008]. It should be noted that these data sets do not contain any ripple height observations and are limited to wavelength information only.

3.3. Equilibrium Ripple Criterion

[40] Some of the data sources contain measurements of mega ripples with wavelengths of up to 8 m; since this study focuses on wave ripples only any ripples with wavelengths greater than 1.5 m have been excluded from further analysis. A smaller cutoff of 1 m is applied to laboratory data as most of the larger ripples were the result of scaled experiments carried out at high water temperature (~60°C) [e.g., *Southard et al*., 1990; *Dumas et al*., 2005]. The following criteria were used to ensure that the data used represent equilibrium conditions with the flow. Since laboratory experiments are run until the ripples no longer show any significant change, any laboratory experiments with a Shields parameter greater than the critical Shields parameter for sediment motion ($\theta_{1/3} > \theta_{cr}$), we assumed represent ripples in equilibrium with the flow. For field conditions, where an objective definition of equilibrium is difficult without information of the time history of the ripple evolution, only ripple data corresponding to $\theta_{1/3} > 2\theta_{cr}$ are considered to be in equilibrium. For the cases where time history of the ripple evolution is known (*Traykovski et al*. [1999], Tr, and the data discussed in section 3.2), equilibrium ripples were identified as those recorded during periods where the hydrodynamic forcing (i.e., excess Shields parameter) does not change significantly over the time required for a ripple to adjust itself to the given hydrodynamic forcing. This corresponds to the time scale (T_k) given

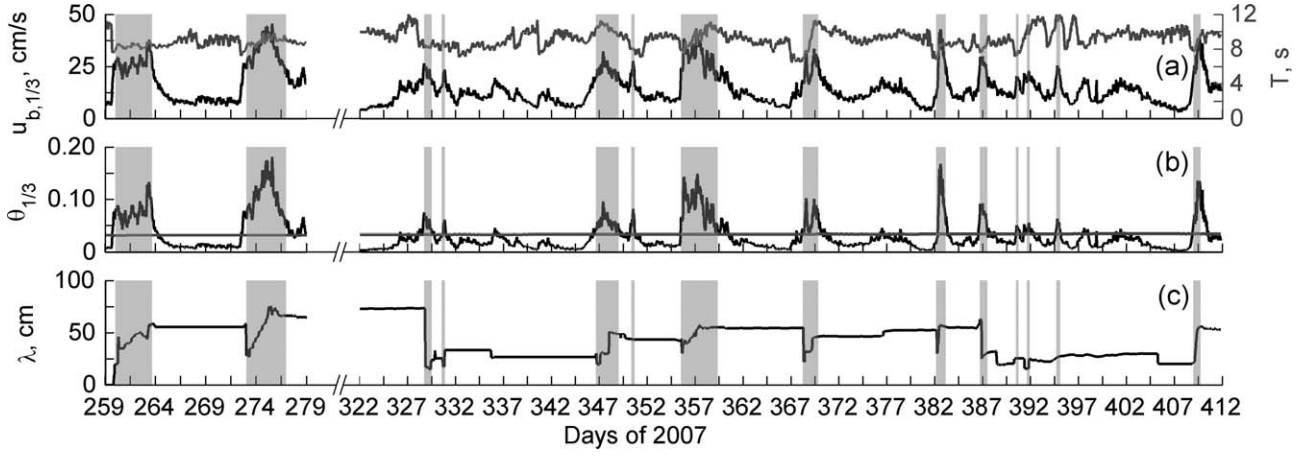

Figure 2. Time series of data collected in the South Atlantic Bight off Georgia (USA) during 2007–2008: (a) significant wave orbital velocity (black) and wave period (gray); (b) wave Shields parameter (black) and critical Shields parameter (gray); and (c) measured ripple wavelength. The shaded areas indicate periods when $0 < d\theta/dt < 0.1\theta_{1/3}(t)/T_k(t)$ and $\theta_{1/3} > 1.5\theta_{cr}$ (see text).

by Tr [equation (9)], and it is a function of the Shields parameter ($\theta_{1/3}$). Thus, only ripple data corresponding to conditions where $0 < d\theta_{1/3}/dt < 0.1\theta_{1/3}(t)/T_k(t)$ are assumed to be in equilibrium with the flow. A further criterion of $\theta_{1/3} > 1.5\theta_{cr}$ was applied to eliminated low-energy conditions where the bed may only experience intermittent sediment mobilization during a wave group and hence would require more time than what the time scale T_k predicts.

[41] The database developed from all sources of data described in the previous two sections includes ripple data from experiments conducted with both regular/monochromatic waves and irregular/random waves, with the former consisting of data from laboratory experiments only. After applying the wavelength and equilibrium criteria, the regular wave data set left consists of 1145 measurements of wavelength and 1049 measurements of ripple steepness. The irregular wave data set consists of all field data and a few laboratory experiments (see Table 3) resulting in 1765 measurements of wavelength and 699 measurements of ripple steepness. The distribution of ripple dimensions (height and wavelength), hydrodynamic conditions (wave period, orbital velocity and bottom excursion), and grain sizes incorporated in this data set is shown in Figure 3. The combination of regular and irregular wave data results in a total of 2910 measurements of ripple wavelength and 1748 measurements of ripple steepness.

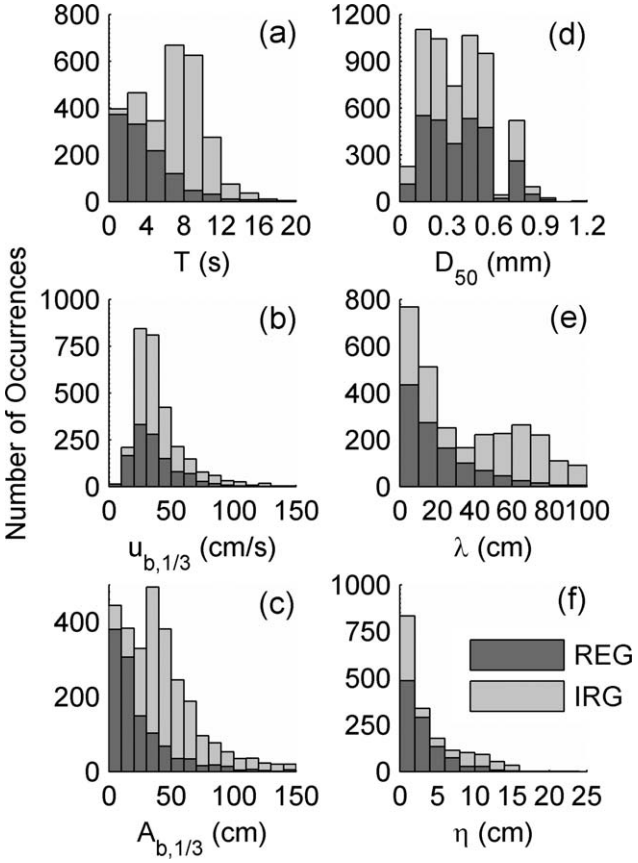

Figure 3. Frequency distribution of range of values for parameters representing hydrodynamic forcing and ripple dimensions for the ripple data sets compiled for this study ($N = 2968$). Data corresponding to regular (REG) and irregular (IRG) conditions are shown as stacked bars. For symbols see text.

4. Results

[42] In this section, all previously published and the newly collected data that have passed the equilibrium criteria are used to evaluate the predictors presented in section 2.

4.1. Mobility Number Based Equilibrium Models

[43] The predictions of equilibrium ripple length, height, and steepness using the mobility number based models (i.e., NF, NL, Vr, and GK) are plotted against the observations in Figure 4. All ripple dimensions have been normalized by the bottom orbital semiexcursion ($A_{b,1/3}$).

[44] It is worth noting that all four models converge for $\psi_{1/3} < 10$ predicting a nearly constant value, indicating a sole dependence of ripple dimensions on A_b. However, this trend is not supported by the data, which show a gradually increasing λ/A_b ratio for decreasing $\psi_{1/3}$. The ripple wavelength data (see Figure 4a) suggest either an inverse relationship between normalized wavelength and $\psi_{1/3}$ or a constant value that should be larger than that predicted by these models. For $\psi_{1/3} > 10$, the models start deviating from each other with the irregular wave data suggesting two trends. One trend follows the predictors of NL, Vr, and to an extent, that of GK while the remaining data follow that of NF and yield a smaller $\lambda/A_{b,1/3}$ ratio value for the same $\psi_{1/3}$. This deviation was also noted by *Nielsen* [1981], who attributed it to differences between laboratory/regular versus field/irregular waves. However, this is not the case in here, as ripples under different wave forcings appear to follow either trend without a specific reference to regular/irregular forcing or sediment size.

[45] The normalized ripple height (see Figure 4b) also follows the trend of decreasing $\eta/A_{b,1/3}$ with increasing $\psi_{1/3}$,

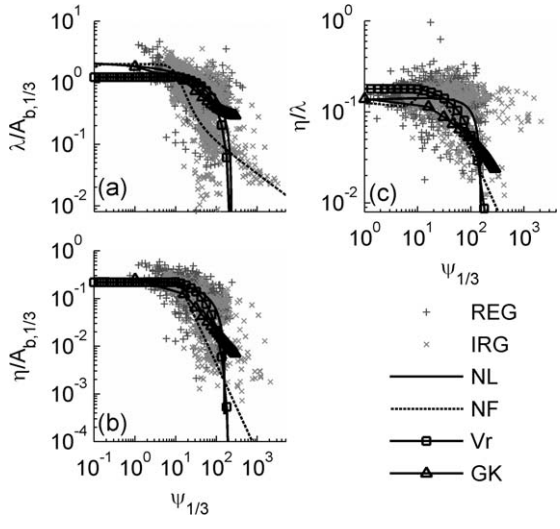

Figure 4. Scatterplot of (a) normalized ripple wavelength ($\lambda/A_{b,1/3}$), (b) normalized ripple height ($\eta/A_{b,1/3}$), and (c) ripple steepness (η/λ) against mobility number ($\psi_{1/3}$). *Key*: REG, regular wave ripples; IRG, irregular wave ripples; NL, *Nielsen* [1981] model for REG waves; NF, *Nielsen* [1981] model for IRG waves; Vr, *Van Rijn* [1993] model; GK, *Grasmeijer and Kleinhans* [2004] model.

although there are fewer measurements for height than for wavelength. All of the predictors fail to yield an accurate ripple height for larger values of $\psi_{1/3}$. NF predicts a smaller height than observed, while NL and Vr yield a flat bed at these larger values and the GK method yields increasing and exceptionally large ripple heights (for $\psi_{1/3} > 900$). The steepness of these ripples estimated from the individual predictions of η and λ (see equations (3)–(6)) is shown in Figure 4c, whereas with wavelength and height, two trends emerge. One trend suggests a nearly constant steepness of $\sim$0.15, for $\psi_{1/3}<10$ which is successfully predicted by the models. However, there is significant scatter at larger values of $\psi_{1/3}$ with some ripples maintaining a steepness of $\sim$0.15, while others show a decrease in steepness with higher values of $\psi_{1/3}$. There is no clear distinction between regular and irregular wave-induced ripples.

4.2. Mobility Number and Sediment Parameter

[46] Both predictors of WM and SG, based on the ratio of the mobility number to the nondimensional sediment parameter, are shown in Figure 5. This ratio reduces some of the scatter and the dual trend in ripple wavelength observed with the predictors presented in the previous section. This is attributed mainly to the fact that this formulation accounts for differences in sediment size found in the data. The overall trend is a decreasing λ/A_b value for increasing ratio of ψ/S_*, with a greater rate of decrease for $\psi_{rms}/S_* > 3$ for WM and $\psi_{eq}/S_* > 2$ for SG. However, while the ripples tend to scale with ψ/S_*, the cutoff values of two and three used by these models are too small as the data suggest values between eight and nine. For nondimensional height, both predictors capture the slope of the data for $\psi_{rms}/S_* > 3$ and $\psi_{eq}/S_* > 2$, while for smaller values of ψ/S_*, the predictors overestimate the rate of decrease. Ripple steepness (Figures 6c and 6f) suggests that some ripples maintain a nearly constant steepness between 0.15 and 0.20, while the remaining ripple data show evidence of a decreasing η/λ for increasing ψ/S_*. The ripple steepness converges around 0.15 for small ψ/S_* but begins to diverge and scatter over an order of magnitude for $\psi/S_* > 2$. The WM predictor assumes a constant η/λ for $\psi_{rms}/S_* < 2$ which agrees with the data, while SG predicts an increasing steepness for decreasing ψ_{eq}/S_* which is not observed. Both WM and SG were only validated over a range of ψ/S_* limited by the available data as shown by the short predicted lines.

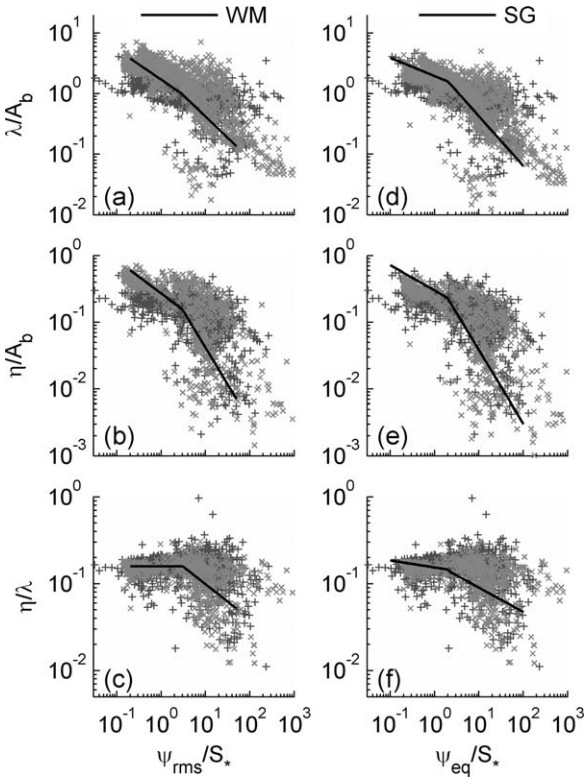

Figure 5. (a–c) Evaluation of the WM ripple predictor where A_b and ψ are calculated using the *rms* wave orbital velocity. (d–f) Evaluation of the SG ripple predictor where A_b and ψ are calculated using the equivalent wave orbital velocities (see text for details). Symbols + and × represent ripple data under REG and IRG wave conditions, respectively.

4.3. Shields Parameter

[47] While *Nielsen* [1981] found ripple wavelength and height to vary as a function of the mobility number, he also noted that steepness is better described by the Shields parameter (Figure 6). As with his equations for λ and η, he found a disparity between ripples under regular and irregular waves, and he established two different equations to describe the observed measurements. However, as shown in Figure 6, these equations fail to accurately describe the observed trend. Similar to the dependence on the mobility number, the steepness follows two trends: constant and decreasing with increasing Shields parameter. Both predictors indicate a flatbed near a Shields parameter value of one, which agrees with some of the data, but ripples clearly remain present at least up to Shields parameter values of 10.

[48] When using the GM model formulations the observations (Figure 7) show no clear trend when $S_* \leq 5$; for $S_* > 5$ the data plot together but they do not segregate as predicted by the GM equation. Better agreement is found

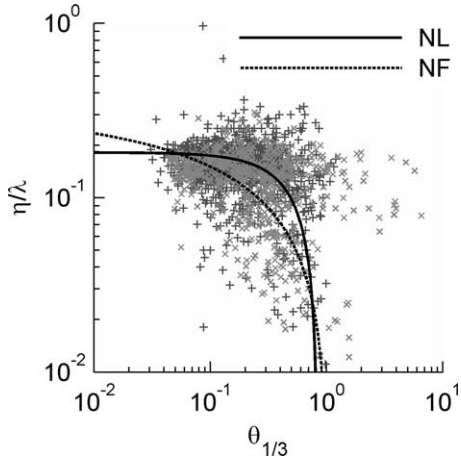

Figure 6. Scatterplot of ripple steepness (η/λ) as a function of the Shields parameter ($\theta_{1/3}$) for data collected under REG (+) and IRG (×) wave conditions. The *Nielsen* [1981] ripple steepness predictions for REG (solid line) and IRG waves (dashed line) are also shown.

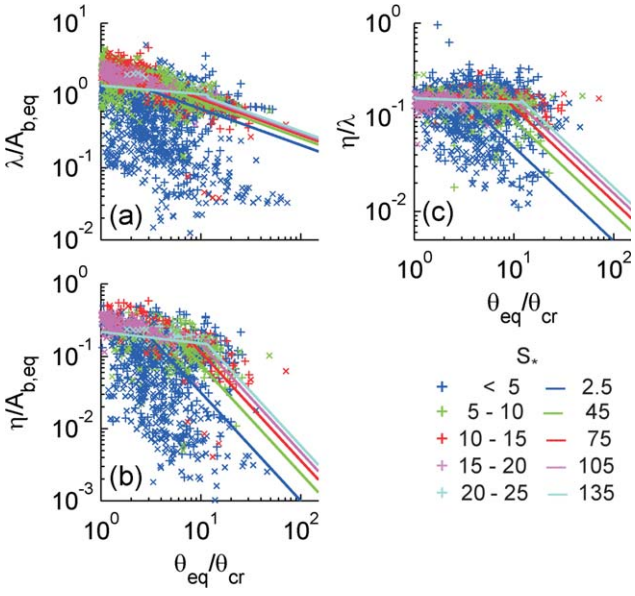

Figure 7. Scatterplot of (a) normalized ripple wavelength ($\lambda/A_{b,eq}$), (b) normalized ripple height ($\eta/A_{b,eq}$), and (c) ripple steepness (η/λ) against the ratio of θ_{eq}/θ_{cr} for REG (+) and IRG (×) wave conditions. The corresponding predictions based on the GM for the various ranges of sediment parameter (S_*) are also shown.

for regular wave data although a significant amount of scatter is still notable. Ignoring data with $S_* \leq 5$, both the observed and predicted trends indicate a nearly constant to gradually decreasing $\lambda/A_{b,eq}$ for $\theta_{eq}/\theta_{cr} < 5$. For $\theta_{eq}/\theta_{cr} > 5$, the dimensionless ripple geometry decreases. The GM prediction for $\lambda/A_{b,eq}$ agrees with that observed with the exception of the data not segregating by S_*. The ripple height as a function of θ_{eq}/θ_{cr} gradually decreases (on a log-log scale), and it does not follow the predicted ripple height of GM. As noted previously, the ripple steepness follows two trends, however, for $S_* > 5$, the majority of the ripple data suggest a constant steepness for increasing θ_{eq}/θ_{cr}.

4.4. Period Parameter

[49] MO model (see Figure 8) appears to be successful in providing the upper limits for both wavelength and ripple height. However, the assumption of constant value of λ/D_{50} for $\chi < 1.4 \times 10^{-7}$ in equation (24) (see dashed line in Figure 8a) does not seem to be supported by the data.

4.5. Orbital Excursion

[50] The predictors of WH and *Soulsby and Whitehouse* [2005] are both based on variations of the wave orbital excursion and are shown against the data in Figure 9. The WH predictor (based on $2A_{b,1/3}/D_{50} = d_{o,1/3}/D_{50}$) captures the general trend of the data (although a high scatter is noted for larger values of $2A_{b,1/3}/D_{50}$ (see Figure 9, left column)). The normalized wavelength (λ/D_{50}, Figure 9a) data for regular waves continue to follow the orbital trend well into the suborbital and anorbital regimes. If these data are excluded, the predicted characteristics for suborbital and anorbital ripples agree with the observed data. However, the regular wave data tend to have smaller λ/D_{50} ratios

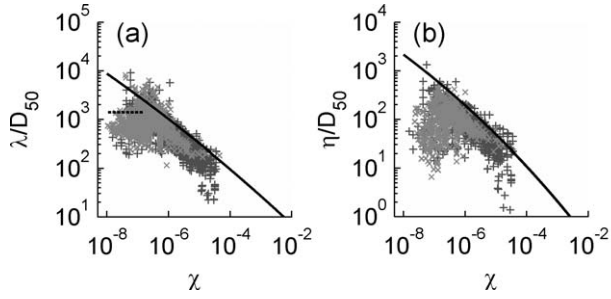

Figure 8. Scatterplot of (a) normalized ripple wavelength (λ/D_{50}) and (b) height (η/D_{50}) plotted against the parameter χ (see equations (22) and (23)) for REG (+) and IRG (×) wave conditions. The maximum equilibrium ripple conditions from the MO equations are also shown as solid lines. The dashed line indicates the equation for field wave conditions (equation (23)) when $\chi < 1.5 \times 10^{-7}$.

than the irregular ones, for the same $2A_{b,1/3}/D_{50}$ values. Therefore, the predictor appears to slightly overpredict regular and underpredict irregular wave ripple dimensions. For normalized ripple height (η/D_{50}, Figure 9b), the regular and irregular wave ripple dimensions agree with the equations

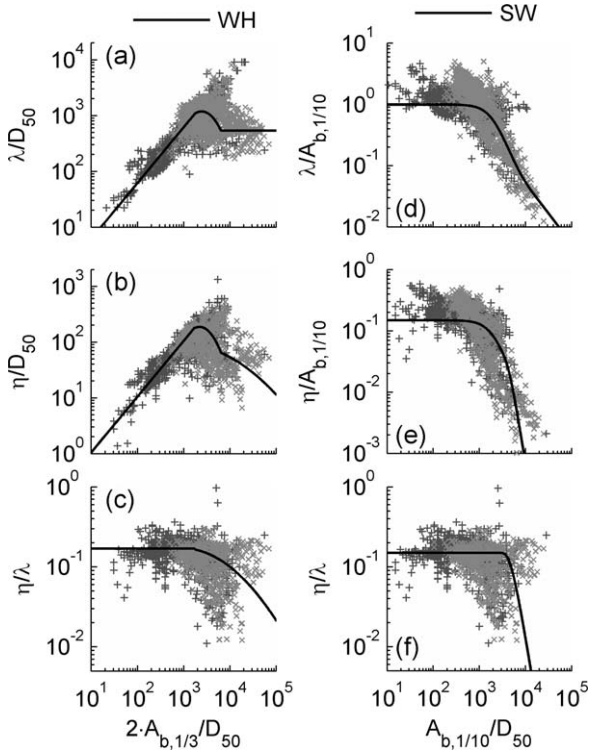

Figure 9. (a–c) Scatterplots of normalized ripple wavelength (λ/D_{50}), height (η/D_{50}), and ripple steepness (η/λ) against normalized wave excursion ($2A_{b,1/3}/D_{50}$) as in the model of WH. (d–f) Scatterplots of normalized ripple wavelength ($\lambda/A_{1/10}$), height ($\eta/A_{1/10}$), and ripple steepness (η/λ) against normalized wave excursion ($A_{b,1/10}/D_{50}$) as in the model of SW. Solid lines show the predictions of the respective models, while data points with the symbols + and × represent ripple geometry data under REG and IRG wave conditions, respectively.

for orbital ripples, however, as with wavelength, some data continue along the trend for larger $2A_{b,1/3}/D_{50}$ ratios. For suborbital ripples, the equations closely follow that of the data but tend to overpredict the regular wave data. For anorbital ripples, η/D_{50} scatters over an order of magnitude around the predicted dimensions. The ripple steepness (Figure 9c) still shows the dual trend observed in the previous predictors.

[51] The SW predictor closely follows the trend of regular wave data for $A_{b,1/10}/D_{50} < 10^3$ (Figure 9, right column). For $A_{b,1/10}/D_{50} > 10^3$ the data follow two trends; that of fairly constant λ/D_{50} ($\approx$1), and that, supported by the bulk of the data, of a gradually decrease in normalized wavelengths, as predicted by the equation. This decreasing trend also follows the measured irregular wave data; however, it does not follow a constant $\lambda/A_{b,1/10}$ for $A_{b,1/10}/D_{50} < 10^3$ but continues to increase. The predicted normalized ripple height shows a rapid decrease in $\eta/A_{b,1/10}$ with increasing $A_{b,1/10}/D_{50}$, while the data scatter exhibit a distribution very similar in shape with that of $\lambda/A_{b,1/10}$ but reduced by a factor of $\sim$10, something that suggests constant ripple steepness. As with other methods, the ripple steepness calculated from the predicted dimensions follows the same trend of being constant initially and decreasing for increasing forcing. *Soulsby et al.* [2012] argue that their predictor worked best for a wide range of the published data; however, although it does appear to reduce the error for many conditions, it ultimately fails to predict ripple height and steepness.

4.6. Orbital Excursion and w_s/ω

[52] In Figure 10, we see that the Tr predictor is able to capture the overall ripple wavelength and height (and consequently steepness) trend, although the data scatter around the model is higher for $u_{b,1/3}/w_s > 4.2$ (Figures 10d–10f) than for $u_{b,1/3}/w_s < 4.2$ (see Figure 10a). A better agreement (less scatter) is found with the irregular wave data than with the regular ones.

4.7. Reynolds Numbers and Mobility Number

[53] The FF equations predict that $\lambda/A_{b,1/3}$ decreases for increasing Re_w and increases for increasing Re_d (see Figure 11). The observed ripple dimensions follow the decreasing $\lambda/A_{b,1/3}$ for increasing Re_w pattern, but the segregation by Re_d suggested by the model is not observable in the data (Figure 11). For ripple height, the observations do not reveal any correlation with Re_w and $\psi_{1/3}$ as suggested by equation (34). Taken as a single equation fit through the scatter the equation might perform well, but the dependence on Re_d and Re_w is not evident. For steepness, FF predicted a value of $\sim$0.18, which plots along the largest steepness observed (Figure 11c), thereby overpredicting the majority of the observations.

4.8. Orbital Velocity, Settling Velocity, and Re_p

[54] The PG equations (37) and (38) provide estimates of ripple dimensions normalized by grain size (see Figure 12). Under this classification, the dimensions for regular and irregular wave data cluster all together; however, the PG predictor estimates do deviate from the observed data. This predictor captures the trend of the data with a decreasing $\lambda/d_{o,1/3}$ and $\eta/d_{o,1/3}$ for increasing $u_{b,1/3}/w_s$, but it either overpredicts or underpredicts, depending on the Re_p value.

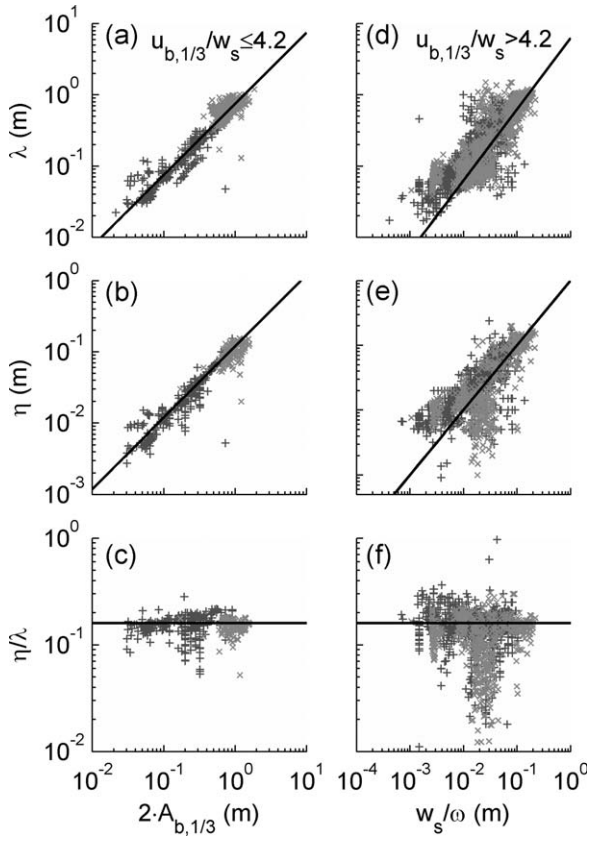

Figure 10. Scatter diagrams of ripple wavelength (λ), height (η), and steepness (η/λ) plotted against wave orbital excursion ($2A_{b,1/3}$) (a–c) and against the ratio of settling velocity (w_s) over wave radial period (ω) (d–f) for data corresponding to conditions $u_{b,1/3} \leq 4.2 \cdot w_s$ and for $u_{b,1/3} > 4.2 \cdot w_s$ as suggested by Tr. Solid lines denote the predictions of the Tr model. Data points with the symbols + and × represent ripple geometry data under REG and IRG wave conditions, respectively.

When $Re_p \geq 13$, the data scatter show the $\lambda/d_{o,1/3}$ ratio to decrease at larger rate for smaller $u_{b,1/3}/w_s$ values than the equation predicts. This leads to underprediction for small and overprediction at larger $u_{b,1/3}/w_s$ values. Ripple steepness is poorly captured by this predictor, as the observations suggest a constant value for $u_{b,1/3}/w_s < 0.18$ and a decrease for $u_{b,1/3}/w_s > 0.18$ following local increase at $u_{b,1/3}/w_s \sim 0.18$. When $9 \leq Re_p < 13$ (see Figures 12d–12f), the predictor follows the general trend of the wavelength data only for small $u_{b,1/3}/w_s$ ratios; a better agreement is found with the normalized ripple height data ($\eta/d_{o,1/3}$) and ripple steepness. For $Re_p < 9$ (Figures 12g–12i), the predictor underpredicts both normalized ripple wavelength and height. The same applies for steepness as the observations follow only a weak decreasing trend and scatter almost as much along the $u_{b,1/3}/w_s$ axis as in η/λ.

5. Discussion

[55] The qualitative comparison between the newly created ripple geometry database and the predictors presented in section 2 confirmed the widespread differences in

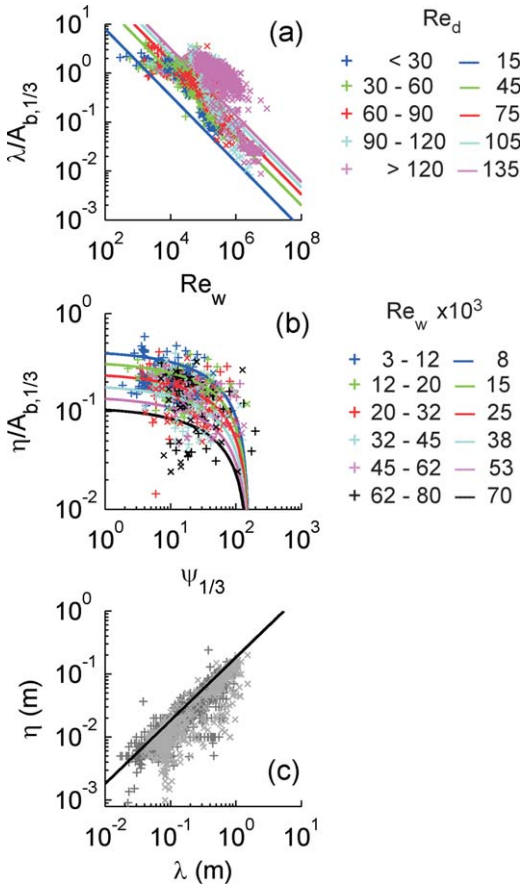

Figure 11. Scatter diagrams of (a) normalized ripple wavelength ($\lambda/A_{b,1/3}$) against wave Reynolds number (Re_w); (b) normalized ripple height ($\eta/A_{b,1/3}$) against the mobility number ($\psi_{1/3}$); and (c) ripple height (η) against ripple wavelength (λ). Solid lines show the predictions of the FF model for the various ranges of sediment (Re_d) and wave (Re_w) Reynolds numbers where a 30° angle of repose is shown in (c) (for details see text). The symbols + and × denote ripple geometry data corresponding to REG and IRG wave conditions, respectively.

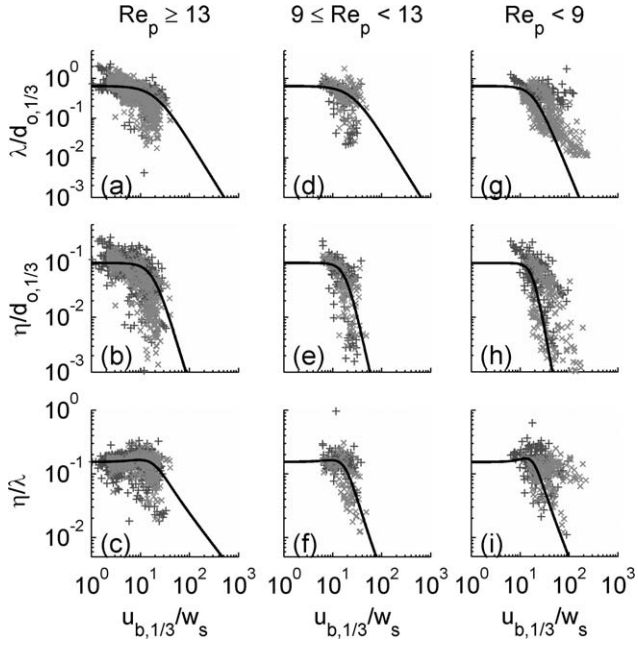

Figure 12. Scatterplots of ripple dimensions normalized by the wave orbital excursion ($d_{o,1/3}$) and ripple steepness against the ratio of wave orbital velocity over sediment settling velocity ($u_{b,1/3}/w_s$) for the various ranges of particle Reynolds number (Re_p) as suggested by the PG equilibrium model (equations (37) and (38)) of PG. The symbols + and × denote data collected under REG and IRG waves, respectively.

performance. Some of the presented models failed to agree well with the data under large wave forcing conditions. In terms of wavelength, this was particularly the case for the Vr and GK equations. Vr used his data set to determine that a flatbed should occur at a mobility number of 250 and therefore derived an equation where the ripple geometry goes to zero at this value. However, the data set (see Figure 4) confirms the existence of ripples even when the mobility number value exceeds 250. Establishment of an accurate cutoff between a rippled and flat bed is not pursued here, as the goal is to have a predictor capable of predicting dimension over the whole range of conditions observed in this data set. The failure of the GK predictor is attributed mainly to the fact that the polynomial equation describing the model yields increasing and exceptionally large values for mobility numbers greater than 900. Similarly, the predictors of *Nielsen* [1981] were introduced for $\theta_{1/3} < 1$, as above this value *Nielsen* [1981] suggested the transition to a flat bed. However, in our data set we can see ripples being present for $\theta > 1$ so we have not imposed this condition on the *Nielsen* [1981] models either. For ripple height, the predictors of NL, FF, GK, and the *Nielsen* [1981] for steepness have not shown a good agreement with the data especially under large wave forcing. These limitations suggest that these predictors might not be suitable for use under all conditions but limited to cases with small mobility number and shear stress values only.

[56] Throughout our comparison of models and data, a different response was present for monochromatic and irregular wave forcing. This explains some of the diverging trends observed in predictors such as SW and MO as well as in the original development of the two different predictors by *Nielsen* [1981]. Assuming that hydrodynamic processes are represented correctly by the corresponding hydrodynamic parameters, the geometry of the ripples should not be significantly different for monochromatic and random wave fields. This motivated SW and PG to create a single predictor which incorporates both laboratory and field data. For the same wave parameters, different ripple characteristics might occur depending on the nature of the waves (i.e., directional spectral characteristics), their complexity (i.e., velocity asymmetry, acceleration skewness), and potential superposition of mean flows. However, these differences should not create significantly different ripple geometries as those identified in the data. This is investigated by initially examining the regular and irregular wave data sets separately.

5.1. Ripple Wavelength

[57] Ripple wavelength is a quantity approximately 10 times larger than ripple height. Therefore, ripple wavelength

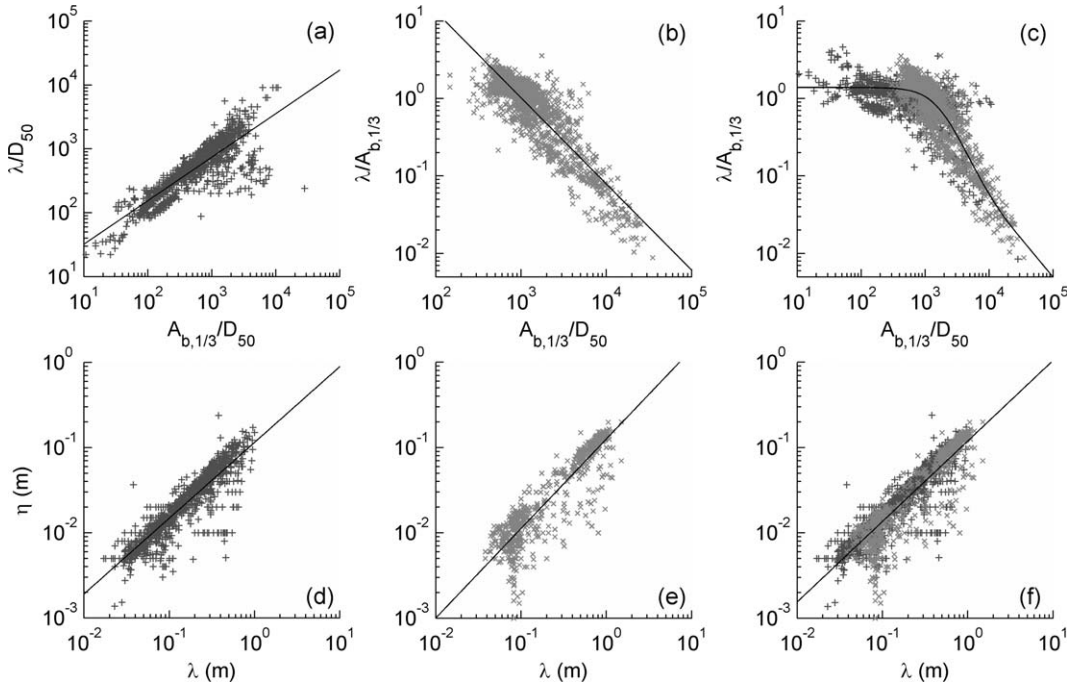

Figure 13. (top) Scatterplots of (a) ripple wavelength (λ) normalized by particle size (D_{50}) for REG wave conditions (equation (42)); (b) ripple wavelength (λ) normalized by wave semiorbital excursion ($A_{b,1/3}$) for IRG wave conditions (equation (43)); and (c) the same as (b) but with all data combined (CMB; equation (44)). (bottom) Scatterplots of ripple height (η) versus wavelength (λ) for (d) REG wave (equation (45)), (e) IRG wave (equation (46)), and (f) both REG and IRG wave conditions (equation (49)).

measurements are expected to be more accurate than measurements of ripple height. Furthermore, qualitatively predictors such as that of WH and SW (see Figure 9) that relate ripple wavelength to the ratio of semiorbital excursion (A_b) over median grain size (D_{50}) provided the best agreement with the enriched database. This is explored in Figure 13 where we plot normalized ripple wavelength against the ratio of $A_{b,1/3}/D_{50}$ for regular (Figure 13a) and irregular (Figure 13b) wave conditions. The ripple wavelength normalization is done using mean particle size for irregular waves and wave excursion for regular waves. A clear linear trend (on a log-log scale) is identified between normalized ripple wavelengths and normalized wave excursion although the slopes of the two linear trends are opposite to each other, while the correlation coefficients (r^2) are 0.73 and 0.78 for regular and irregular wave forcing, respectively. A least squares fitting on a log-log scale produces the following statistical models for normalized ripple wavelengths for regular waves (Figure 13a):

$$\lambda/D_{50} = 6.76\left(A_{b,1/3}/D_{50}\right)^{0.68} \tag{40}$$

and for irregular waves:

$$\lambda/A_{b,1/3} = 2.22 \times 10^3 \left(A_{b,1/3}/D_{50}\right)^{-1.11} \tag{41}$$

[58] Solving these equations for ripple wavelength, we obtain

$$\lambda = 6.76 A_{b,1/3}^{0.68} D_{50}^{0.32} \tag{42}$$

$$\lambda = 2.22 \times 10^3 \cdot A_{b,1/3}^{-0.11} D_{50}^{1.11} \tag{43}$$

for ripples under regular and irregular wave forcing, respectively. Equation (42) clearly shows that for regular waves, orbital semiexcursion is the dominant parameter controlling ripple wavelength, while for irregular waves (equation (43)) the median grain diameter is the dominant scaling factor. Based on the range of $A_{b,1/3}/D_{50}$ values found in our data sets (10–10^4 for regular waves, 10^2 to 5×10^5 for irregular waves), the monochromatic wave conditions extend to typically orbital scale ripples ($A_{b,1/3}/D_{50} < 877$) with some suborbital ($877 < A_{b,1/3}/D_{50} < 2794$) which partially explains the greater dependence on semiexcursion. On the other hand, ripples formed by irregular waves fall in the suborbital and anorbital ($A_{b,1/3}/D_{50} > 2794$) regimes where grain size becomes more important. However, at the overlapping suborbital region, the data from the monochromatic wave conditions (Figure 13a) trend in agreement with equation (42) well into the suborbital regime, while irregular wave formed ripples continue on an opposing trend into the orbital regime (see Figure 13b). One explanation for the scaling differences between these two types of waves is the consistency of the forcing present. Under monochromatic waves, the bed is subjected to the same orbital excursion with each passing wave, while under irregular waves the orbital excursion varies for each wave. Thus, the grain size acts as a filter and a limiting factor preventing or delaying the transition from suborbital to orbital scaling.

[59] The best attempt to collapse both regular and irregular data using a common parameterization is achieved when we plot $\lambda/A_{b,1/3}$ versus $A_{b,1/3}/D_{50}$ (see Figure 13c) in a similar manner as in SW. Comparing our enriched data

set to that used by SW, we see that our data set includes significantly more field observations with smaller $A_{b,1/3}/D_{50}$ values that allow to define the trend of ripple characteristics over a larger range. Least squares fit, on a log-log scale, of an equation similar to that of SW (equation (27)) through our expanded data set leads to

$$\lambda/A_{b,1/3} = \left(0.72 + 2.0 \times 10^{-3} A_{b,1/3}/D_{50}\left\{1 - \exp\left[-\left(1.57 \times 10^{-4} A_{b,1/3}/D_{50}\right)^{1.15}\right]\right\}\right)^{-1} \quad (44)$$

with a correlation coefficient (r^2) of 0.73. This equation captures the data trend for values of $A_{b,1/3}/D_{50} < 7000$ but may overpredict irregular wave ripples at larger $A_{b,1/3}/D_{50}$ values.

5.2. Ripple Height and Steepness

[60] During the comparison of the data with existing predictors (see section 4), there were a number of occasions where ripple steepness appeared to be constant for a large range of values of the parameter used in the x axis. Similar to wavelength, ripple steepness data (note that the new data set described in section 3.2 did not include ripple heights) are examined for monochromatic and irregular wave conditions, separately. A log-log scatterplot of ripple height versus wavelength shows a linear trend. Least squares analysis on the data reveals the following best fit relationships for regular (Figure 13d) and irregular (Figure 13e) wave conditions:

$$\eta = 0.115\lambda^{0.89} \quad (45)$$

$$\eta = 0.126\lambda^{1.05} \quad (46)$$

with correlation coefficients (r^2), on a log-log scale, of 0.78 and 0.81, respectively. It should be noted that in the above equations both η and λ are in meters. Dividing both parts by wavelength, the following relationships for wave steepness are established

$$\eta/\lambda = 0.115\lambda^{-0.11} = 0.093 A_{b,1/3}^{-0.075} D_{50}^{-0.035} \quad (47)$$

$$\eta/\lambda = 0.126\lambda^{0.05} = 0.185 \times 10^{-2} A_{b,1/3}^{-0.006} D_{50}^{0.056} \quad (48)$$

for regular and irregular wave conditions, respectively. The data and equations (47) and (48) suggest that ripples formed under irregular wave conditions are slightly steeper (0.126) than those formed under regular wave conditions (0.115) with both having an almost constant steepness. The scatter of data points under the predicted line in Figure 13e is attributed to large errors associated with the measurements of very small ripple height ($\eta < 1$ mm) in the field and is considered to represent the experimental error. Unlike for wavelength, when the two data sets are overlaid (see Figure 13f), they collapse on a single trend and least squares fitting produces the following steepness relationship:

$$\eta/\lambda = 0.120\lambda^{-0.056} \quad (49)$$

with a correlation coefficient r^2 of 0.79. The small correction for very long wavelengths is attributed to the enhanced turbulence at the crests due to flow contraction over the ripples [*Du Toit and Sleath*, 1981; *Nielsen*, 1992]. Since ripple height increases with increasing wavelength, the enhancement will be greater for larger ripples.

5.3. Model Errors

[61] The performance of the new models described in equations (40)–(49) is compared to that of all previously presented models (see section 2). For each model, the predicted ripple wavelength and height values are compared against the measured ones from the database; the scatterplots together with the 1:1 line are shown in Figures 14 and 15 for ripple wavelength and height, respectively. The least squares error of each predictor (in a log-log scale) was estimated using the root-mean-square (RMS) error, normalized by the range of the observed values for each parameter predicted:

$$\varepsilon = \frac{\sqrt{\frac{1}{N} \cdot \sum \left(\log_{10}(X_p) - \log_{10}(X_m)\right)^2}}{\left|\log_{10}(\max(X_m)) - \log_{10}(\min(X_m))\right|} \quad (50)$$

where X is the parameter evaluated (i.e., ripple wavelength, height, and steepness), while the subscripts m and p denote measured and predicted values, respectively. The errors associated with the existing ripple predictors and the newly developed ones (see equations (40)–(49)) are listed in Table 4. The error analysis was performed for all data collected under regular and irregular waves separately but also on the combined data set.

[62] Under regular waves, equations (44) and (49) yield the least error ($\varepsilon = 0.10$), despite the fact that they have been developed using the irregular wave data set. It is characteristic that the WH and the SW predictors provide good agreements with the data as they are also based on the ratio A_b/D_{50}, with their errors being only 0.11. Equations (42) and (45) developed from the regular wave data provide an error similar to that of WH and SW ($\varepsilon = 0.11$).

[63] For irregular wave ripples, the corresponding equations (43) and (46) and equations (44) and (49) developed using all data, as well as the WH model provides the least error ($\varepsilon = 0.15$).

[64] Comparing against the whole data set (combined data), neither the equations for regular nor irregular waves perform as well ($\varepsilon = 0.13$ and 0.17, respectively) as those developed using these data (equations (44) and (49)), which together with the WH equation, yield the smallest average error ($\varepsilon = 0.11$). The disparity between these models is mainly due to the different scaling of ripple wavelength between regular and irregular wave conditions. The former ripples scale with semiorbital excursion length, while the latter ones scale with the particle size.

[65] Overall, the newly developed predictors provide the least normalized RMS errors for most of the cases, with that of WH emerging as the second best. The strong performance of the newly developed models is not surprising as this is the only model that has been developed using the whole data set assembled in this database.

[66] It should be pointed out that equations (44) and (49) yield an identical mean error to the WH predictor, for both the irregular wave and the combined data sets ($\varepsilon = 0.15$ and $\varepsilon = 0.11$, respectively). These same equations perform

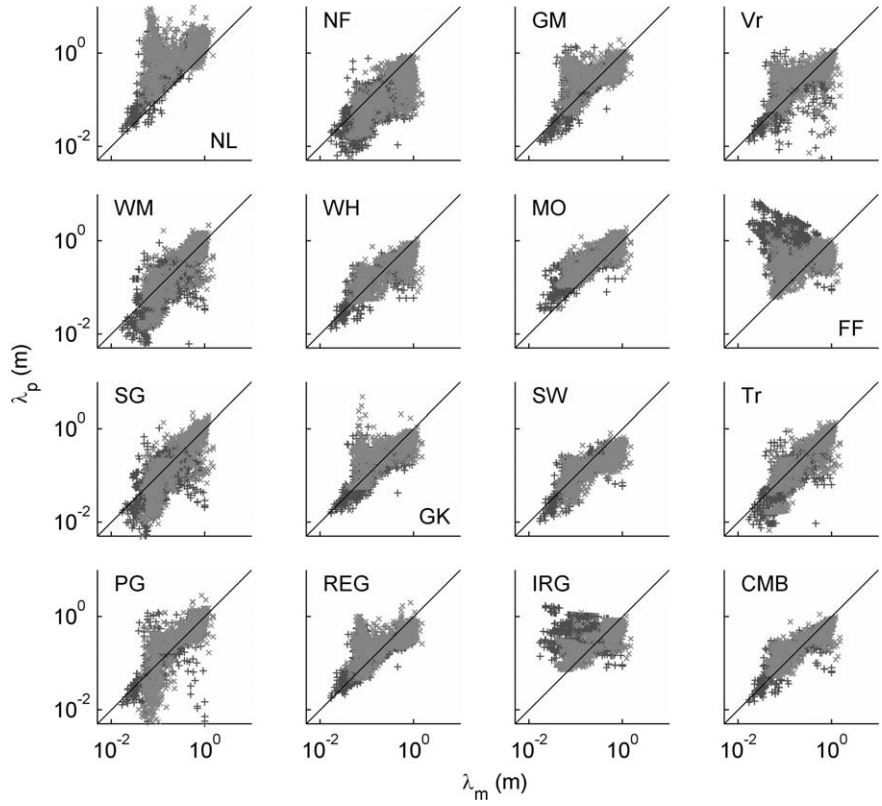

Figure 14. Comparison of predicted (λ_p) versus measured (λ_m) ripple wavelengths for the various models examined in this study (see Table 2) and equations (42)–(44) developed using data from REG, IRG, and CMB wave conditions. Light and dark gray symbols represent data from IRG and REG wave conditions, respectively.

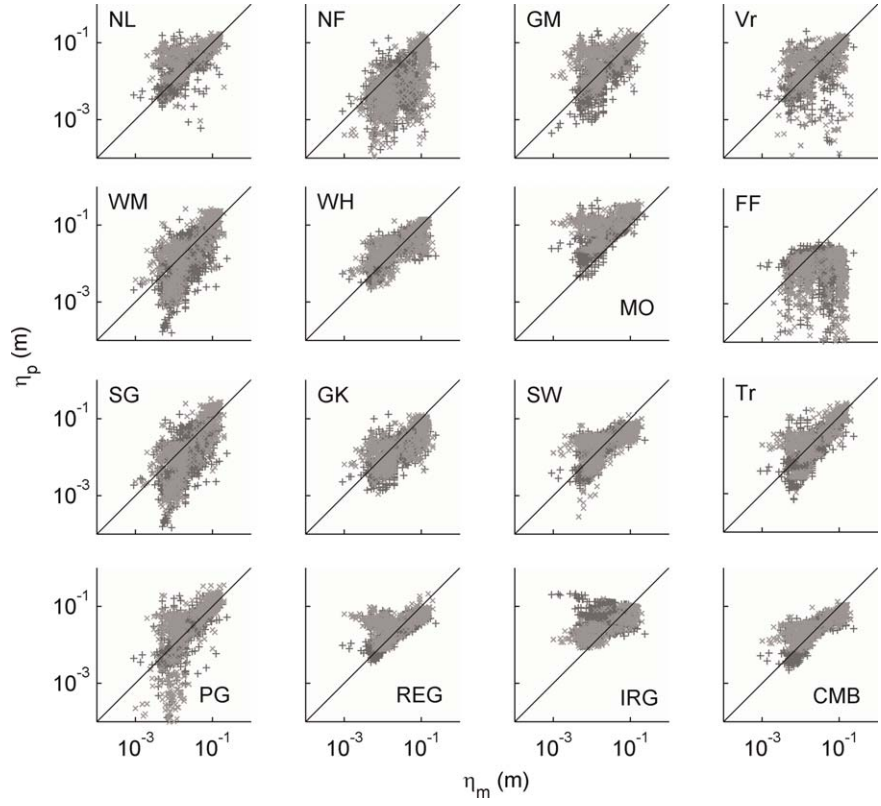

Figure 15. Comparison of predicted (η_p) versus measured (η_m) ripple height for the various models examined in this study (see Table 2) and equations (45), (46), and (49) developed using data from REG, IRG, and all (CMB) wave conditions. Light and dark gray symbols represent data from IRG and REG wave conditions, respectively.

Table 4. Normalized RMS Errors[a] Between Measurements and Predictions[b]

	REG Waves				IRG Waves				CMB			
	ε_λ	ε_η	$\varepsilon_{\eta/\lambda}$	Mean	ε_λ	ε_η	$\varepsilon_{\eta/\lambda}$	Mean	ε_λ	ε_η	$\varepsilon_{\eta/\lambda}$	Mean
NL	0.24	0.12	0.88	0.41	0.39	0.22	1.11	0.57	0.28	0.15	0.85	0.43
NF	0.27	0.27	0.14	0.22	0.24	0.32	0.25	0.27	0.22	0.28	0.16	0.22
GM	0.14	0.14	0.13	0.14	0.23	0.20	0.19	0.21	0.16	0.17	0.13	0.15
Vr	0.17	0.19	0.14	0.17	0.23	0.43	0.32	0.33	0.18	0.27	0.18	0.21
WM	0.21	0.21	0.12	0.18	0.15	0.18	***0.16***	0.16	0.16	0.20	0.12	0.16
WH	0.13	0.10	***0.09***	0.11	0.14	0.15	***0.16***	***0.15***	0.12	0.12	***0.10***	***0.11***
MO	0.18	0.20	0.15	0.18	0.18	0.31	0.35	0.28	0.16	0.24	0.20	0.20
FF	0.55	0.32	0.12	0.33	0.21	0.55	0.22	0.33	0.34	0.38	0.13	0.28
SG	0.23	0.22	0.12	0.19	0.16	0.20	***0.16***	0.17	0.17	0.21	0.12	0.16
GK	0.13	0.16	0.14	0.14	0.18	0.17	0.24	0.20	0.14	0.16	0.15	0.15
SW	***0.12***	0.10	0.10	0.11	0.24	0.18	0.19	0.20	0.17	0.14	0.11	0.14
Tr	0.18	0.13	0.10	0.13	0.14	0.16	0.19	0.16	0.14	0.14	0.11	0.13
PG	0.19	0.17	0.11	0.16	0.20	0.31	0.28	0.26	0.17	0.23	0.15	0.18
Equations (42) and (45)	***0.12***	0.11	***0.09***	0.11	0.21	0.20	0.17	0.19	0.15	0.15	***0.10***	0.13
Equations (43) and (46)	0.34	0.21	0.10	0.22	0.14	***0.14***	***0.16***	***0.15***	0.22	0.18	0.11	0.17
Equations (44) and (49)	***0.12***	***0.09***	0.10	***0.10***	***0.13***	0.15	0.17	***0.15***	***0.11***	***0.11***	0.11	***0.11***

[a]Smallest error values are shown in bold italic fonts.
[b]See text for details.

better than WH for regular wave conditions. In terms of ripple wavelength, equations (44) and (49) yield the best predictions, for all three conditions, while for ripple height, these equations are as good as WH for the irregular wave, and better than any other model for the regular and combined data sets. Furthermore, equation (44) is in a simpler and easier to apply form, whereas the WH predictor requires an iterative or a multistep approach [*Malarkey and Davies*, 2003].

6. Conclusions

[67] In this contribution, an extensive database of ripple dimensions was assembled that includes existing data from published literature and two additional field sites. After processing for uniformity in the parameters used to describe hydrodynamic conditions, the data are tabulated and made available for the community in electronic form (see supporting information).

[68] Our analysis showed that ripple steepness is a relatively constant number that slightly increases for decreasing ripple length. This applies for both regular and irregular wave conditions, and it can be collapsed into a single model (equation (49)). According to this model, ripple steepness is 0.12 at large wavelengths ($\sim$1 m) increasing by approximately 29% (to 0.15) for ripples with a wavelength of only 1 cm.

[69] For all practical applications, the equilibrium wavelength is better scaled by wave semiorbital excursion rather than by particle size, and it can be predicted by equation (44). This is similar to the equation presented by SW but with the fitting parameters defined from a larger range of experimental data. For field applications, with $A_{b,1/3}/D_{50}$ ratios smaller than 1000, equation (43) is recommended.

[70] Ripple height can be predicted from wave steepness (equation (49)), after the wavelength has been estimated from either equation (43) or (44).

[71] The WH predictor also provides good agreement with this extensive data set; however, the simplicity of this new model might make its application more attractive for inclusion in numerical models or in time-dependent ripple dimension prediction models.

[72] Finally, we should emphasize that these predictors provide equilibrium ripple conditions, which could resemble real ripple conditions only if enough time has lapsed for the ripples to adjust to the prevailing hydrodynamic forcing. Experience has shown that these dimensions might be close to reality during increasing hydrodynamic forcing; they can deviate from reality during periods of descending wave energy as in such cases relic ripples dominate the environment.

[73] **Acknowledgments.** Financial support for this work was provided by the National Science Foundation (NSF awards OCE-0451989 and OCE-0535893) and by the South Carolina Coastal Erosion Project, a cooperative study supported by the U.S. Geological Survey and the South Carolina Sea Grant Consortium (Sea Grant Project R/CP-11).

References

Ardhuin, F., Drake, T. G., and T. H. C. Herbers (2002), Observations of wave-generated vortex ripples on the North Carolina continental shelf, *J. Geophys. Res.*, *107*(C10), 3143, doi:10.1029/2001JC000986.

Ardhuin, F., O'Reilly, W. C., Herbers, T. H. C, and P. F. Jessen (2003), Swell transformation across the continental shelf. Part I: Attenuation and directional broadening, *J. Phys. Oceanogr.*, *33*, 1921–1939.

Bagnold, R. A. (1946), Motion of waves in shallow water. Interaction between waves and sand bottoms, *Proc. R. Soc. Lond. Ser. A: Math. Phys. Sci.*, *187*, 1–18.

Bosman, J. J. (1981), Bed behaviour and sand concentration under oscillatory water motion, *Rep. on Model Invest. M 1695 Part 1*, Delft Hydraul. Lab., Delft, Netherlands.

Boyd, R., Forbes, D. L., and D. E. Heffler (1988), Time-sequence observations of wave-formed sand ripples on an ocean shoreface, *Sedimentology*, *35*, 449–464, doi:10.1111/j.1365-3091.1988.tb00997.x.

Brown, J. (2006), *Sea-bed response to non-breaking waves*, BS dissertation, Ohio State Univ., Columbus.

Carstens, M. R., Neilson, F. M., and H. D. Altinbilek (1969), *Bed forms generated in the laboratory under an oscillatory flow: Analytical and experimental study*, Tech. Memo. 28, 105 pp., U.S. Army Corps of Eng., Coastal Eng. Res. Cent., Vicksburg, Miss.

Chotiros, N. P., Smith, E., and J. N. Piper (2002), Refraction and scattering into a sandy ocean sediment in the 30–40-kHz band, *IEEE J. Ocean. Eng.*, *27*(3), 362–375.

Clifton, H. E. (1976), Wave-formed sedimentary structures: A conceptual model, in *Beach and Nearshore Sedimentation*, edited by R. A. Davis Jr. and R. L. Ethington, Spec. Publ. SEPM Soc. Sediment. Geol. *24*, pp. 126–148.

Clifton, H. E., and J. R. Dingler (1984), Wave-formed structures and paleoenvironmental reconstruction, *Mar. Geol.*, *60*, 165–198, doi:10.1016/0025-3227(84)90149-X.

Collins, M. B. and G. Voulgaris (1993), Empirical field and laboratory evaluation of a real-time acoustic sea bed surveying system, *Proc. Inst. Acoust.*, *15*(2), 343–351.

Dietrich, W. E. (1982), Settling velocity of natural particles, *Water Resour. Res.*, *18*, 1615–1626, doi:10.1029/WR018i006p01615.

Dingler, J. (1974), Wave-formed ripples in nearshore sands, PhD dissertation, Univ. of Calif., San Diego.

Doucette, J. S. (2000), The distribution of nearshore bedforms and effects on sand suspension on low-energy, micro-tidal beaches in southwestern Australia, *Mar. Geol.*, *165*(1), 41–61, doi:10.1016/S0025-3227(00)00002–5.

Doucette, J. S. (2002), Geometry and grain-size sorting of ripples on low-energy sandy beaches: Field observations and model predictions, *Sedimentology*, *49*(3), 483–503, doi:10.1046/j.1365-3091.2002.00456.x.

Doucette, J. S., and T. O'Donoghue (2006), Response of sand ripples to change in oscillatory flow, *Sedimentology*, *53*(3), 581–596, doi:10.1111/j.1365-3091.2006.00774.x.

Du Toit, C. G., and J. F. Sleath (1981), Velocity measurements close to rippled beds in oscillatory flow, *J. Fluid Mech.*, *112*, 71–96, doi:10.1017/S002211208100030X.

Dumas, S., Arnott, R. W. C., and J. B. Southard (2005), Experiments on oscillatory-flow and combined-flow bed forms: implications for interpreting parts of the shallow-marine sedimentary record, *J. Sediment. Res.*, *75*(3), 501–513, doi:10.2110/jsr.2005.039.

Faraci, C., and E. Foti (2001), Evolution of small scale regular patterns generated by waves propagating over a sandy bottom, *Phys. Fluids*, *13*, 1624–1634, doi:10.1063/1.1367871.

Faraci, C., and E. Foti (2002), Geometry, migration and evolution of small-scale bedforms generated by regular and irregular waves, *Coastal Eng.*, *47*(1), 35–52, doi:10.1016/S0378–3839(02)00097-2.

Gibbs, R. J., Matthews, M. D., D. A. Link (1971), The relationship between sphere size and settling velocity, *J. Sediment. Res.*, *41*(1), 7–18, doi:10.1306/74D721D0-2B21-11D7-8648000102C1865D.

Grant, W. D., and O. S. Madsen (1982), Movable bed roughness in unsteady oscillatory flow, *J. Geophys. Res.*, *87*(C1), 469–481, doi:10.1029/JC087iC01p00469.

Grant, W. D., and O. S. Madsen (1986), The continental-shelf bottom boundary layer, *Annu. Rev. Fluid Mech.*, *18*(1), 265–305, doi:10.1146/annurev.fl.18.010186.001405.

Grasmeijer, B. T., and M. G. Kleinhans (2004), Observed and predicted bed forms and their effect on suspended sand concentrations, *Coastal Eng.*, *51*(5), 351–371, doi:10.1016/j.coastaleng.2004.05.001.

Grasmeijer, B. T., and L. C. van Rijn (1999), Transport of fine sands by currents and waves. III: Breaking waves over barred profile with ripples, *J. Waterw. Port Coastal Ocean Eng.*, *125*(2), 71–79, doi:10.1061/(ASCE)0733-950X(1999)125:2(71).

Hanes, D. M., Alymov, V., Chang, Y. S., and C. Jette (2001), Wave-formed sand ripples at Duck, North Carolina, *J. Geophys. Res.*, *106*(C10), 22,575–22,592, doi:10.1029/2000JC000337.

Hay, A. E., and D. J. Wilson (1994), Rotary sidescan images of nearshore bedform evolution during a storm, *Mar. Geol.*, *119*(1), 57–65, doi:10.1016/0025-3227(94)90140-6.

Hayakawa, N., Tsujimoto, G., and H. Hashimoto (1983), Velocity distribution and suspended sediment concentration over large-scale ripples, *Coastal Eng. Jpn.*, *26*, 91–100.

Horikawa, K., and A. Watanabe (1967), A study on sand movement due to wave action, *Coastal Eng. Jpn.*, *10*, 39–57.

Huettel, M., Ziebis, W., Forster, S., and G. W. Luther III (1998), Advective transport affecting metal and nutrient distributions and interfacial fluxes in permeable sediments, *Geochim. Cosmochim. Acta*, *62*(4), 613–631, doi:10.1016/S0016-7037(97)00371-2.

Hume, T. M., Green, M. O., and J. W. Oldman (1999), What happens at the seabed off a headland during a tropical cyclone, in *Coastal Sediments (1999)*, edited by N. C. Kraus and W. G. McDougal, Reston, VA., United States. ASCE, pp. 1836-1851.

Inman, D. L. (1957), *Wave-generated ripples in nearshore sands*, Rep. TM-100, Scripps Inst. of Oceanogr., La Jolla, Calif.

Jackson, D. R., Williams, K. L., Thorsos, E. I., and S. G. Kargl, S. G. (2002), High-frequency subcritical acoustic penetration into a sandy sediment, *IEEE J. Ocean. Eng.*, *27*(3), 346–361, doi:10.1109/JOE.2002.1040923.

Jonsson, I. G. (1966). Wave boundary layers and friction factors, Proc. Coastal Eng., *1*(10), Tokyo, Japan, doi:10.9753/icce.v10.

Kennedy, J. F., and M. Falcon (1965), *Wave-Generated Sediment Ripples*, Rep. 86, Hydrodyn. Lab., Dep. of Civ. Eng., Mass. Inst. of Technol.

Khelifa, A., and Y. Ouellet (2000), Prediction of sand ripple geometry under waves and currents, *J. Waterw. Port Coastal Ocean Eng.*, *126*(1), 14–22, doi:10.1061/(ASCE)0733–950X(2000)126:1(14).

Komar, P. D. (1974), Oscillatory ripple marks and the evaluation of ancient wave conditions and environments, *J. Sediment. Res.*, *44*(1), 169–180.

Li, M. Z., C. L. Amos (1998), Predicting ripple geometry and bed roughness under combined waves and currents in a continental shelf environment, *Cont. Shelf Res.*, *18*(9), 941–970, doi:10.1016/S0278-4343(98)00034-X.

Lofquist, K. E. (1978). Sand ripple growth in an oscillatory-flow water tunnel, Rep. CERC-TP-78-5, Coastal Eng. Res. Cent., Fort Belvoir, Va.

Madsen, O., Negara, A., Lim, K., and H. Cheong (2010), Near-bottom flow characteristics of currents at arbitrary angle to 2D ripples, Proc. Coastal Eng., *1*(32), 12 pp., doi:10.9753/icce.v32.currents.36.

Malarkey, J., and A. G. Davies (2003), A non-iterative procedure for the Wiberg and Harris (1994) oscillatory sand ripple predictor, *J. Coastal Res.*, *19*(3), 738–739.

Miller, M. C., and P. D. Komar (1980), A field investigation of the relationship between oscillation ripple spacing and the near-bottom water orbital motions, *J. Sediment. Res.*, *50*(1), 183–191.

Mogridge, G. R. (1972), Wave generated bed forms, PhD dissertation, Dep. of Civ. Eng., Queen's Univ., Kingston, Vancouver, Canada.

Mogridge, G. R., and J. W. Kamphuis (1972), Experiments on bed form generation by wave action, Proc. Coastal Eng., *1*(13), 1123–1142, doi:10.9753/icce.v13.

Mogridge, G. R., Davies, M. H., and D. H. Willis (1994), Geometry prediction for wave-generated bedforms, *Coastal Eng.*, *22*(3), 255–286, doi:10.1016/0378-3839(94)90039-6.

Nielsen, P. (1979), Some basic concepts of wave sediment transport, *Ser. Pap. 20*, Tech. Univ. of Denmark, Inst. of Hydrodyn. and Hydraul. Eng., Lyngby, Denmark.

Nielsen, P. (1981), Dynamics and geometry of wave-generated ripples, *J. Geophys. Res.*, *86*(C7), 6467–6472, doi:10.1029/JC086iC07p06467.

Nielsen, P. (1984), Field measurements of time-averaged suspended sediment concentrations under waves, *Coastal Eng.*, *8*(1), 51–72, doi:10.1016/0378-3839(84)90022-X.

Nielsen, P. (1992), *Coastal Bottom Boundary Layers and Sediment Transport*, World Sci., Singapore.

Nielsen, P., Svendsen, I., and C. Staub (1978), Onshore-offshore sediment movement on a beach, Proc. Coastal Eng., *1*(16), doi:10.9753/icce.v16.

Nieuwjaar, M., and T. Van der Kaay (1987), *Sediment concentration and transport in case of irregular non-breaking waves with a current*, Delft Tech. Univ., Civ. Eng. Dep., Delft, Netherlands.

O'Donoghue, T., and G. S. Clubb (2001), Sand ripples generated by regular oscillatory flow, *Coastal Eng.*, *44*(2), 101–115, doi:10.1016/S0378–3839(01)00025-4.

O'Donoghue, T., J. S. Doucette, J. J. Van der Werf, and J. S. Ribberink (2006), The dimensions of sand ripples in full-scale oscillatory flows, *Coastal Eng.*, *53*(12), 997–1012, doi:10.1016/j.coastaleng.2006.06.008.

Pedocchi, F., and M. H. García (2009a), Ripple morphology under oscillatory flow: 1. Prediction, *J. Geophys. Res.*, *114*, C12014, doi:10.1029/2009JC005354.

Pedocchi, F., and M. H. García (2009b), Ripple morphology under oscillatory flow: 2. Experiments, *J. Geophys. Res.*, *114*, C12015, doi:10.1029/2009JC005356.

Powell, H., Voulgaris, G., Collins, M. B., and A. C. Bastos (2000), Wave-current interaction over bedforms: observations and model predictions, Mar. Sandwave Dyn., March 23–24 2000, Lille *1* University, Lille, France, edited by A. Trentesaux and T. Garlan, pp. 153–160.

Precht, E., and M. Huettel (2004), Rapid wave-driven advective pore water exchange in a permeable coastal sediment, *J. Sea Res.*, *51*, 93–107, doi:10.1016/j.seares.2003.07.003.

Ribberink, J. S., and A. A. Al-Salem (1994), Sediment transport in oscillatory boundary layers in cases of rippled beds and sheet flow, *J. Geophys. Res.*, *99*(C6), 12,707–12,727, doi:10.1029/94JC00380.

Ribberink, J., and L. C. van Rijn (1987), Influence of wave-asymmetry and wave-irregularity on time and bed averaged sediment concentrations, Rep. H186-00-1, Delft Hydraul., Delft, Netherlands.

Rocha, C. (2008), Sandy sediments as active biogeochemical reactors: compound cycling in the fast lane, *Aquat. Mictob. Ecol.*, *53*, 119–127, doi:10.3354/ame01221.

Sakakiyama, T., T. Shimizu, R. Kajima, S. Saito, and K. Maruyama (1986), Sand ripples generated by prototype waves in a large wave flume, *Coastal Eng. Jpn.*, *28*, 147–160.

Schwab, W. C., et al. (2009), *Coastal change along the shore of northeastern South Carolina—The South Carolina Coastal Erosion Study*, edited by W. A. Barnhardt, USGS Circ. 1339, 77 pp.

Shields, A. (1936), Application of similarity principles and turbulence research to bed-load movement, *Commun. Prussian Lab. of Hydraul.*, *26*, Prussian Lab. of Hydraul., Berlin, Germany.

Sleath, J., and S. Wallbridge (2002), Pickup from rippled beds in oscillatory flow, *J. Waterw. Port Coastal Ocean Eng.*, *128*, 228–237, doi:10.1061/(ASCE)0733-950X(2002)128:6(228).

Smith, D., and J. F. A. Sleath (2005), Transient ripples in oscillatory flows, *Cont. Shelf Res.*, *25*, 485–501, doi:10.1016/j.csr.2004.10.012.

Soulsby, R. L., and R. J. S. Whitehouse (2005), Prediction of ripple properties in shelf seas, mark 2 predictor for time evolution, *Tech. Rep. TR 154 Release 2.0*, HR Wallingford, Wallingford, U. K.

Soulsby, R. L., Whitehouse, R. J. S., and K. V. Marten (2012), Prediction of time-evolving sand ripples in shelf seas, *Cont. Shelf Res*, *38*, 47–62, doi:10.1016/j.csr.2012.02.016.

Southard, J. B., Lambie, J. M., Federico, D. C., Pile, H. T., and C. R. Weidman (1990), Experiments on bed configurations in fine sands under bidirectional purely oscillatory flow, and the origin of hummocky cross-stratification, *J. Sediment. Res.*, *60*(1), 1–17.

Sullivan, C. M., Warner, J. C., Martini, M. A., Voulgaris, G., Work, P. A.; Haas, K. A., and D. Hanes (2006) South Carolina Coastal Erosion Study, data report for observations, October 2003–April 2004, USGS Open-File Rep. 2005-1429.

Steetzel, H. J. (1984), Near bottom sediment suspension under oscillatory water motion, MSc dissertation, Civ. Eng. Dep. Coastal Div., Tech. Univ. Delft, Delft, Netherlands.

Styles, R., and S. M. Glenn (2002), Modeling bottom roughness in the presence of wave-generated ripples, *J. Geophys. Res.*, *107*(C8), 3110, doi:10.1029/2001JC000864.

Thorne, P. D., J. J. Williams, and A. G. Davies (2002), Suspended sediments under waves measured in a large-scale flume facility, *J. Geophys. Res.*, *107*(C8), 3178, doi:10.1029/2001JC000988.

Thorsos, E. I., and M. D. Richardson (2002), Guest editorial, *IEEE J. Ocean. Eng.*, *27*(3), 341–345, doi:10.1109/JOE.2002.1040922.

Traykovski, P. (2007), Observations of wave orbital scale ripples and a nonequilibrium time-dependent model, *J. Geophys. Res.*, *112*(C06026), doi:10.1029/2006JC003811.

Traykovski, P., Hay, A. E., Irish, J. D., and J. F. Lynch (1999), Geometry, migration, and evolution of wave orbital ripples at LEO-15, *J. Geophys. Res.*, *104*(C1), 1505–1524, doi:10.1029/1998JC900026.

Van Rijn, L. C. (1987), Database sand concentration profiles for currents and waves, Tech. Rep. M 1695-04, Delft Hydraul., Delft, Netherlands.

Van Rijn, L. C. (1993), *Principles of Sediment Transport in Rivers*, Estuaries and Coastal Seas, Aqua Publ., Amsterdam, Netherlands.

Van Rijn, L. C., and F. J. Havinga (1995), Transport of fine sands by currents and waves: II. *J. Waterw. Port Coastal Ocean Eng.*, *121*(2), 123–133, doi:10.1061/(ASCE)0733-950X(1995)121:2(123).

Van Rijn, L. C., Nieuwjaar, M. W., van der Kaay, T., Nap, E., and A. van Kampen (1993), Transport of fine sands by currents and waves, *J. Waterw. Port Coastal Ocean Eng.*, *119*(2), 123–143, doi:10.1061/(ASCE)0733–950X(1993)119:2(123).

Voulgaris, G., and J. P. Morin (2008), A long-term real time sea bed morphology evolution system in the South Atlantic Bight, in Current Measurement Technology, 2008, CMTC 2008, IEEE/OES 9th Working Conference, IEEE, pp. 71–79, doi:10.1109/CCM.2008.4480847.

Voulgaris, G., Collins, M. B., Davis, J., and M. Wilkin (1992), RoxAnn sea bed discrimination system: In situ and laboratory evaluation, Tech. Rep. SUDO/TEC/92/4C, Dep. of Oceanogr., Univ. of Southampton, U. K.

Warner, J. C., B. Armstrong, C. S. Sylvester, G. Voulgaris, T. Nelson, W. C. Schwab, and J. F. Denny (2012), Storm-induced inner-continental shelf circulation and sediment transport: Long Bay, South Carolina, *Cont. Shelf Res.*, *42*, 51–63, doi:10.1016/j.csr.2012.05.001.

Wiberg, P. L., and C. K. Harris (1994), Ripple geometry in wave-dominated environments, *J. Geophys. Res.*, *99*(C1), 775–789, doi:10.1029/93JC02726.

Wiberg, P. L., and C. R. Sherwood (2008), Calculating wave-generated bottom orbital velocities from surface wave parameters, *Comput. Geosci.*, *34*(10), 1243–1262, doi:10.1016/j.cageo.2008.02.010.

Wikramanayake, P. N., and O. S. Madsen (1994), Calculation of movable bed friction factors, Tech. Rep. DRP-94-5, Coastal Eng. Res. Cent., U.S. Army Corps of Eng., Vicksburg, Miss.

Williams, J. J., Bell, P. S., Thorne, P. D., Trouw, K., Hardcastle, P. J., and J. D. Humphery (2000), Observed and predicted vertical suspended sediment concentration profiles and bedforms in oscillatory-only flow, *J. Coastal Res.*, *16*(3), 698–708.

Williams, J. J., Bell, P. S., Thorne, P. D., Metje, N., and L. E. Coates (2004), Measurement and prediction of wave-generated suborbital ripples, *J. Geophys. Res.*, *109*(C2), C02004, doi:10.1029/2003JC001882.

Willis, D. H., Davies, M. H., and G. R. Mogridge (1993), Laboratory observations of bedforms under directional irregular waves, *Can. J. Civ. Eng.*, *20*(4), 550–563, doi:10.1139/l93-072.

Xu, J. P. (2005), Observations of plan-view sand ripple behavior and spectral wave climate on the inner shelf of San Pedro Bay, California, *Cont. Shelf Res.*, *25*(3), 373–396, doi:10.1016/j.csr.2004.10.004.

Yalin, S., and R. Russell (1962), Similarity in sediment transport due to waves, in *Proceedings of the 8th International Conference on Coastal Engineering*, Mexico City, Mexico, doi:10.9753/icce.v8.12.